



HAL
open science

On the relationship between water vapour field evolution and the life cycle of precipitation systems

Joël van Baelen, M. Reverdy, F. Tridon, L. Labbouz, G. Dick, M. Bender, M.

Hagen

► To cite this version:

Joël van Baelen, M. Reverdy, F. Tridon, L. Labbouz, G. Dick, et al.. On the relationship between water vapour field evolution and the life cycle of precipitation systems. Quarterly Journal of the Royal Meteorological Society, 2011, Advances in the understanding of convective processes and precipitation over low-mountain regions through the Convective and Orographically-induced Precipitation Study (COPS), 137 (S1), pp.204-223. 10.1002/qj.785 . hal-01893745

HAL Id: hal-01893745

<https://uca.hal.science/hal-01893745>

Submitted on 11 Oct 2018

HAL is a multi-disciplinary open access archive for the deposit and dissemination of scientific research documents, whether they are published or not. The documents may come from teaching and research institutions in France or abroad, or from public or private research centers.

L'archive ouverte pluridisciplinaire **HAL**, est destinée au dépôt et à la diffusion de documents scientifiques de niveau recherche, publiés ou non, émanant des établissements d'enseignement et de recherche français ou étrangers, des laboratoires publics ou privés.



On the relationship between water vapour field evolution and precipitation systems lifecycle

Journal:	<i>QJRMS</i>
Manuscript ID:	QJ-10-0070.R2
Wiley - Manuscript type:	Research Article
Date Submitted by the Author:	n/a
Complete List of Authors:	Van Baelen, Joel; LaMP / OPGC Reverdy, Mathieu; LaMP/OPGC Labbouz, Laurent; LaMP/OPGC Tridon, Frédéric; LaMP/CNRS Dick, Galina; Helmholtz Centre Potsdam, German Research Centre for Geosciences Bender, Michael; Helmholtz Centre Potsdam Hagen, Martin; DLR
Keywords:	water vapour, GPS tomography, precipitation systems, convective initiation, weather radars

1
2
3
4
5
6
7
8
9 **On the relationship between water vapour field evolution and**
10
11 **Precipitation systems lifecycle**
12
13

14
15
16 Van Baelen^{1*}, J., M. Reverdy¹, F. Tridon¹, L.Labbouz¹,

17
18 G. Dick², M. Bender², and M.Hagen³
19
20

- 21
22
23 1) Laboratoire de Météorologie Physique, CNRS – University Blaise Pascal, Clermont-Fd, France
24
25 2) Helmholtz-Centre Potsdam, GFZ, German Research Center for Geosciences, Potsdam, Germany
26
27 3) Deutsches Zentrum für Luft- und Raumfahrt (DLR), Oberpfaffenhofen, Germany
28
29
30
31
32
33
34
35

36 Manuscript prepared for the COPS special issue of the
37
38 Quarterly Journal of the Royal Meteorological Society
39

40 31 October 2010
41
42
43
44
45
46
47
48
49

50 Corresponding author address:

51 LaMP, Université Blaise Pascal, 24 Avenue des Landais, P.O. Box 80026, 63171 Aubière CEDEX, France

52
53 E-mail : j.vanbaelen@opgc.univ-bpclermont.fr
54
55
56
57
58
59
60

Abstract

In this work, we investigate the relationship that can be found between precipitation systems structure and evolution, from initiation to decay, and the associated water vapour field distribution during the COPS (Convective Orographically-induced Precipitation Study) international field campaign which took place from the Vosges to the Black Forest Mountains, across the Rhine Valley, in summer 2007. In particular, we consider water vapour retrieval through GPS Integrated Water Vapour 2-D maps as well as 3-D tomography and confront it to precipitation systems observed with the ground based C band POLDIRAD weather radar.

On one hand, we have evidenced the predominant role of water vapour as a precursor to convective initiation for local convective cell generation. Water vapour accumulation on the crest of the orography is associated with ridge convection, while water vapour passing over the mountain top and creating valley outflows generates lee side convection often triggered by a small hill positioned within or close to the valley exit, or by a local convergence with the plain water vapour field.

On the other hand, we have noted that frontal systems seemed to develop preferably where the largest amount of water vapour was available. Likewise, in the case of frontal systems, well formed synoptic scale storms are associated with high water vapour signatures, while lighter systems with embedded convection appear to trail high water vapour areas where the convective part is associated with local water vapour depletion. This later aspect could be the signature of the convective cloud formation, when water vapour is transferred into liquid water, before the onset of precipitation.

I/ Introduction

The COPS (Convective Orographically-induced Precipitation Study) international field campaign took place in the summer of 2007 from June to August, in the region of South-West Germany / North-East France, across the Rhine Valley from the Vosges Mountains to the Black Forest Mountains (Figure 1). The overall objective of COPS is to improve the Quantitative Precipitation Forecast (QPF) skill of Numerical Weather Prediction (NWP) models over mid-range mountainous terrain. Hence, the research interests of the campaign deal primarily with the study of the meteorological conditions and forcing mechanisms leading to convective initiation, with the monitoring of the precipitation life cycle, and with the analysis of the role played by orography on initiation and development of the precipitation system. To achieve this goal, a large set of in-situ and remote sensing instrumentation was deployed over a series of super sites at selected locations across the domain of interest, while numerous operational and research models were run operationally to assess their performances with respect to the different events observed during Intensive Operation Periods (IOP's).

For more details on the campaign background, on its implication within other international efforts, on the strategy of the observations and campaign implementation, on the description and characteristics of the instruments deployed, and on some preliminary results, please see Wulfmeyer et al. (2008) and Wulfmeyer et al. (2011). Likewise, reports on results and ongoing research in the framework of COPS can be found in Kottmeier et al. (2008) and in the various papers of this special issue.

The scientific scope of the present paper only tackles a small aspect of this ambitious program. It focuses on the preliminary investigation of the relationship that can be found between the

1
2
3
4
5
6 precipitation system structure, intensity and dynamics, from initiation to decay, and the
7 associated water vapour field distribution and evolution. In particular, we will consider water
8 vapour retrieval exclusively through GPS tomography and precipitation systems monitoring with
9 ground based radars only. At this point we easily acknowledge that this provides only a partial
10 view of the problem, while further investigations using increased resolution and other means of
11 measurements are still in progress. Nonetheless, the underlying questions of the current work
12 deal with the role of water vapour as a precursor and/or tracer of precipitation activity, with the
13 effect of orography on the water vapour field distribution and evolution, with the necessity (or
14 not?) of water vapour convergence to start convective activity or foster precipitation system
15 enhancement, etc. but also with the capability of the GPS tomography to provide an adequate
16 tool to study such problems.
17
18
19
20
21
22
23
24
25
26
27
28
29
30
31
32
33

34 In section 2, we will present the experimental set-up deployed during the COPS campaign that
35 provided the data we have used in this study: the GPS network, the POLDIRAD (Polarimetric
36 Diversity Doppler Radar) C- band (~5 GHz) research radar and the French super-site UHF (~1.2
37 GHz) wind profiler. In section 3, we will describe the GPS signal processing as well as the
38 tomography algorithm used and discuss its scope and current limitations. In section 4, we will
39 focus on particular IOP cases where precipitation events were monitored with POLDIRAD to
40 study their associated GPS retrieved water vapour field and its evolution before and during the
41 rain. Finally, in section 5, we will offer some preliminary conclusions and comments, and outline
42 further work and developments.
43
44
45
46
47
48
49
50
51
52
53
54
55
56

57 **II/ The experimental set-up**

58
59
60

1
2
3
4
5
6 For more than a decade, the GPS (Global Positioning System) has proven to be an autonomous,
7
8 all-weather and continuous system for the restitution of the atmospheric water vapour (Bevis et
9
10 al., 1992; 1994; Businger et al., 1996). With such a technique, one can retrieve the IWV
11
12 (Integrated Water Vapour) representative of the atmospheric column above the GPS station with
13
14 good accuracy (Tregoning et al., 1998; Van Baelen et al., 2005; Wang et al., 2007). Furthermore,
15
16 when a dense network of GPS stations exists, GPS can be used to perform tomography in order
17
18 to retrieve the three dimensional distribution of water vapour density (Flores et al, 2000; 2001;
19
20 Gradinarsky and Jarlemark, 2004; Champollion et al., 2005; Reverdy et al., 2009).

21
22 Therefore, as part of the COPS instrumental set-up, the existing networks of GPS stations in
23
24 France and Germany were enhanced with temporary stations such that an average separation of
25
26 less than 40 kilometres between GPS stations over the entire COPS domain was achieved.
27
28 Furthermore, a denser segment of stations separated by about 10 kilometres was also created
29
30 from the crest of the Vosges to the Black Forest, across the Rhine valley. This segment was
31
32 somewhat aligned with the different supersites of the campaign. Figure 1 shows the resulting
33
34 network of GPS stations that provided data for the present work. The stations within the network
35
36 have distributed altitudes, some installed in the plains or valleys, others implemented on the
37
38 mountains to offer a homogenous representation of the varying terrain of the region. Within the
39
40 network, most stations stand between 136 m ASL and 912 m ASL (with the exception of the
41
42 station installed at the Hornisgrinde supersite at 1213 m ASL). For all GPS stations, data were
43
44 recorded with a 30 second sampling interval and an elevation cut-off angle of 5°.

45
46
47
48
49
50
51
52
53
54 In order to relate on the water vapour field evolution and patterns retrieved through GPS
55
56 tomography to the different characteristics of precipitating systems, we use weather radar
57
58
59
60

1
2
3
4
5
6 observations to monitor the convective initiation, the onset of precipitation and the subsequent
7
8 development of those precipitation systems.
9

10
11 The polarimetric C-band Doppler research radar POLDIRAD (Schroth et al., 1988) of DLR
12
13 (Deutsches Zentrum für Luft- und Raumfahrt) was deployed for 3 months in the foothills of the
14
15 Vosges Mountains at Waltenheim-sur-Zorn at 260 m MSL, about 20 km north-west of
16
17 Strasbourg. Its location was about 100 m above the floor of the Rhine Valley providing an
18
19 undisturbed overview over the Rhine Valley, the Black Forest and the Vosges in order to ideally
20
21 complement the existing operational weather radars from Deutscher Wetterdienst, MeteoFrance
22
23 and MeteoSwiss. During IOPs, volume PPI (Plan Position Indicator) scans were performed up to
24
25 120 km range every 10 to 20 minutes.
26
27
28
29
30

31
32 For the COPS campaign, the Vosges supersite also included a UHF boundary layer wind profiler
33
34 fielded by the CNRM (Centre National de Recherches Météorologiques) of Meteo France in the
35
36 plains a few kilometres east of the Vosges foothills (Richard et al., 2009). This radar provides
37
38 vertical profiles of wind amplitude and direction with 75 m height resolution from 150 m above
39
40 the ground up to about 3 km and with a 15 minute time resolution in its high resolution mode.
41
42 However, this wind profiler was only deployed during the month of July.
43
44
45
46
47

48 Figure 1 indicates the locations of the POLDIRAD radar and of the French super-site, where the
49
50 UHF radar was installed.
51
52
53

54 **III/ GPS processing and tomography for water vapour field retrieval**

55
56
57
58
59
60

1
2
3
4
5
6 The GPS data collected throughout the campaign were processed with the EPOS (Earth
7 Parameter and Orbit System) software package developed at the GFZ (GeoForschungZentrum,
8 Potsdam, Germany) (see Gendt et al., 2001, 2004 for detailed description of EPOS). Globally,
9 the EPOS software can estimate different parameters from GPS observations. It can be used for
10 various applications by configuring the processing correspondingly, for example IGS
11 (International GNSS Service) data processing, GPS campaign and GPS meteorology. For GPS
12 meteorological applications, data can be processed in network mode and Precise Point
13 Positioning (PPP) mode (Zumberge et al., 1997) with the EPOS software. In PPP mode, all
14 satellite related parameters, i. e. satellite orbits and clocks, earth rotation parameters, etc. are
15 assumed to be well known, so that there are no common parameter among stations, consequently
16 the data can be processed station by station, i.e. in PPP mode. This enables data of a larger
17 number of GPS stations observed simultaneously, for example, data from a dense network, to be
18 processed independently on different processors and/or computers. In order to obtain the satellite
19 related parameters, a global network should be processed in the similar way as for the generation
20 of the IGS ultra-rapid or rapid products which can usually only be carried out by IGS Analysis
21 Centres like GFZ. Here for regional GPS meteorological applications, to involve some stations
22 around the network will improve the parameters needed to be fixed in PPP data processing.
23 EPOS is based on a least-squares adjustment of zero-differenced phase and range observations.
24 The advantage of using zero-differenced observations is that ray path residuals required to
25 construct the slant total delays (STDs) are available directly in form of observation residuals.
26 For precise positioning the signal delay due to the neutral atmosphere needs to be modelled. The
27 zenith total delay (ZTD) and atmospheric gradients in NS and EW direction are therefore
28 estimated together with the geodetic parameters. The STD along a given signal path can be
29 approximated by applying the Global Mapping Function (GMF) (Boehm et al., 2006) or the Niell
30
31
32
33
34
35
36
37
38
39
40
41
42
43
44
45
46
47
48
49
50
51
52
53
54
55
56
57
58
59
60

1
2
3
4
5
6 mapping function (Niell, 1996) to the ZTDs while the horizontal atmospheric inhomogeneity is
7 provided by the gradients. Hence, contributions to the path delay which cannot be described by
8 this model go into the ray path residuals. To obtain more precise atmospheric parameters the
9 station coordinates and several other parameters are fixed in the troposphere PPP run. Due to the
10 reduced number of free parameters the residuals are dominated by unmodelled atmospheric
11 contributions while the impact of other uncertainties is minimised. Under these assumptions the
12 STD is given by

$$STD = m_h \cdot ZHD + m_w \cdot [ZWD + \cot \varepsilon (G_N \cos \varphi + G_E \sin \varphi)] + \delta$$

23
24
25
26
27
28
29 where the *ZHD* and *ZWD* are the hydrostatic and the wet zenith delay, respectively, m_h and m_w
30 are the hydrostatic and the wet mapping functions, G_N and G_E are the delay gradient parameters
31 in the northern and eastern direction, ε is the elevation, φ is the geographic latitude and δ is the
32 post-fit phase residual. In this automated signal analysis, the hydrostatic and the wet
33 contributions to the ZTD are separated using the Saastamoinen model and climatological data.
34 The zenith delays and mapping functions alone lead to STDs which are rotationally symmetric.
35 The information about spatial atmospheric structures is mainly provided by the residuals and to
36 a minor degree by the gradients.

37
38
39
40
41
42
43
44
45
46
47
48 The errors of the GPS observations and the rather complicated processing chain are difficult to
49 estimate. Therefore, it is important to validate the ZTD and STD estimates with independent
50 observations (Duan et al., 1996; Ware et al., 1997; Liljegren et al., 1999; Braun et al., 2003,
51 Van Baelen et al., 2005) or models (Ha et al., 2003; Liu et al., 2006). Inter-comparison studies
52 with water vapour radiometers and weather models show a STD bias below 1 mm for elevations
53 greater than 30° and below 1.5 mm for elevations down to 5° (Bender et al., 2008).
54
55
56
57
58
59
60

1
2
3
4
5
6 For meteorological applications the availability and the temporal resolution of these data is
7 important. Currently, GPS raw observations with a sampling rate of 2.5 minutes are processed on
8 a hourly basis and the results are available in near real-time. A 12 hour sliding window with 1 h
9 steps is used to process the tropospheric parameters for the most recent hour. Gradients are
10 estimated once per hour, ZTDs for 15 minutes intervals. STDs are retrieved with the full
11 sampling rate of 2.5 minutes by adjusting the corresponding residuals for each individual
12 satellite-receiver link. 96 ZTDs and about 4500 STDs are available per station and day.
13
14
15
16
17
18
19
20
21
22
23

24 For case studies, when an ensemble of GPS stations is available over a limited area, the
25 transmission rays from satellites to receivers can interleave together and tomography inversion
26 will allow the restitution of the three dimensional distribution of the atmospheric water vapour.
27 Indeed, if one defines the volume above the GPS network as an ensemble of atmospheric boxes,
28 called voxels, these voxels will be traversed by the various individual rays. Hence, in this case,
29 the STD's are the GPS observable used for tomography but, first, they have to be converted into
30 SIWVs (Slant Integrated Water Vapour) which correspond to the humidity induced part of the
31 tropospheric delay in the propagation from the satellite to the receiver. To derive the SIWVs
32 from the STDs, one has first to subtract the corresponding hydrostatic part. For precise
33 meteorological analysis, that step requires to determine the pressure field, determined from
34 meteorological surface stations for example, and to calculate the hydrostatic component along
35 each ray, using Saastamoinen's formulation (1972), as it propagates through the atmospheric
36 volume above the analysis domain. Then, following relations defined by Emardson and Dirks
37 (1999) that make use of the atmospheric temperature, the resulting SWD (Slant Wet Delay) can
38 be converted into SIWV. Once these SIWV are determined, they are distributed among the
39 different voxels of the analysis domain, according to the length of their path within each voxel
40
41
42
43
44
45
46
47
48
49
50
51
52
53
54
55
56
57
58
59
60

1
2
3
4
5
6 they cross and weighted by the vertical distribution of the standard atmosphere (i.e., more weight
7
8 to the lower levels where water vapour is more abundant). These lengths are essential to create
9
10 the linear operator of the tomography. Also, we consider that there is no water vapour above an
11
12 altitude of 12km. Likewise, when one of the ray quits the analysis domain through one of the
13
14 side limits of the analysis domain, under 12 kilometres of altitude, it is accounted for only its
15
16 proportional path within the domain as SIWV are integrated values.
17

18
19 Depending on the GPS station and satellite geometry, some voxels will contain data (one or
20
21 multiple rays), especially in the highest layers of the atmosphere, while some others might not, in
22
23 particular in the lowest layers of the grid. Thus, we face a partially determined problem that can
24
25 be written under the following equation [Tarantola, 2005]:
26
27

$$d = G \times m$$

28
29 where d represents the data (SIWV), G the model we will use, i.e the linear operator providing
30
31 the length distribution of SIWV through the voxels and m corresponds to our results, i.e., the
32
33 water vapour density distribution in the voxels. A solution to that linear problem is given by a
34
35 weighted least square fit equation solution (Menke, 1989; Tarantola, 2005):
36
37

$$m^{est} = m_0 + \left(G^t \times W_{GPS} \times G + \alpha^2 \times W_{Model} \right)^{-1} \times G^t \times W_{GPS} \times (d - G \times m_0)$$

38
39 where m_0 is an a priori solution or first guest, W_{GPS} corresponds to the inverse of the
40
41 variance/covariance matrix of the data errors : $W_{GPS} = (C_{GPS})^{-1}$, W_{Model} corresponds to the matrix
42
43 of the variability of the model around the a priori values, G is the model, and α is a weighting
44
45
46
47
48
49
50
51
52
53
54
55
56
57
58
59
60

1
2
3
4
5
6
7 coefficient. In theory, by varying α , one can vary the respective weight on the data or on the a
8
9 priori estimation. The larger the α , the more weight is given to the initialization as a solution and,
10
11 inversely, the lesser the α , the more weight is given to the data. The influence of α is still the
12
13 object of ongoing sensitivity work, so we have chosen here a solution akin of a regular least
14
15 square fit equation by keeping α neutral, i.e. equal to 1. Further details are provided in (Reverdy,
16
17 2008).

18
19 Hence, another important step in the tomography inversion process is to initialize the inversion
20
21 matrix, i.e. provide an “*a priori*” solution. In our case, this is done with a standard atmosphere
22
23 profile, i.e., an exponentially decreasing profile with altitude (McClatchey et al., 1972), adjusted
24
25 to the voxel column IWV derived from the GPS measurements. First, the GPS derived IWV field
26
27 is interpolated through out the analysis domain. Then, for each voxel column, the corresponding
28
29 mean IWV and mean topography are computed. Finally, the standard profile contribution above
30
31 the equivalent altitude is scaled to match the mean GPS derived IWV and reported in the a priori
32
33 solution for the corresponding voxel column. Thus, for the tomography that we have developed
34
35 and implemented here, we rely uniquely on the GPS observables although making use of outside
36
37 sources of information such as radiosondes (Champollion et al., 2009), microwave profiling
38
39 radiometers (MacDonald et al., 2002) or even lidar measurements could easily be adapted and
40
41 will be the object of future work. However, it has been our choice also to restrict the GPS
42
43 tomography by not using external water vapour profiles for two reasons: first, we wanted to
44
45 avoid reducing tomography to merely filling the time steps between successive profiles
46
47 interpolations although we know we will lack vertical structure reconstruction when the spacing
48
49 between GPS stations is too large, and second, the profiles “assimilation” strategies can have a
50
51 significant influence on the resulting fields and we wanted to see how much could be extracted
52
53 from GPS alone.
54
55
56
57
58
59
60

1
2
3
4
5
6
7
8
9
10
11
12
13
14
15
16
17
18
19
20
21
22
23
24
25
26
27
28
29
30
31
32
33
34
35
36
37
38
39
40
41
42
43
44
45
46
47
48
49
50
51
52
53
54
55
56
57
58
59
60

Once the water vapour field is initialized and the SIWV have been adequately distributed among the corresponding voxels, then the tomography resolution is a mere weighted least square equation inversion problem (Reverdy, 2008) where the resulting matrix is the 3-D distribution of water vapour density in the various voxel defined over the analysis domain.

In the case studies presented hereafter, the basic tomography was run with a 14 x 14 x 16 voxel grid covering the COPS area from 47.5° North to 49.5° North and from 6.25° East to 9.25° East, corresponding to a 16 km horizontal resolution with a varying height resolution getting coarser with altitude as water vapour amounts decreases, starting at 500 m height resolution up to 4 km of altitude, increasing to 750 m height resolution up to 7 km of altitude and finally ending at 1000m height resolution up to the maximum analysis height of 12 km of altitude where the water vapour is deemed negligible, and using all of the GPS station data available for the domain shown in Figure 1. For increased resolution and to avoid artefacts due to lack of information brought by excessive spacing between GPS stations, we have also run the tomography analysis on a sub section of the domain where the GPS station density was the largest, from 48.0° North to 48.9° North and from 6.7° East to 8.5° East, with a 12x12x16 voxel grid for an horizontal resolution of about 10 km (8.4 km x 11.2 km) and an unchanged vertical resolution of 500 m in the lower levels.

IV/ Case studies and discussion

In this paper, we have taken the approach to use exclusively GPS IWV fields and tomography water vapour retrieval in conjunction with local radar observations to consider the precipitation systems behaviour. Hence, the case studies will necessarily be limited in their scope as numerous

1
2
3
4
5
6 atmospheric parameters, such as those derived from radiosondes (Convective Available Potential
7 Energy - CAPE, Convective Inhibition - CIN, Richardson number, etc.) or also VERA (Vienna
8 Enhanced Resolution Analysis) (Steinacker et al., 2006) for low level dynamics for example, are
9 not used or accounted for at this time.
10
11
12

13
14 Therefore, in these preliminary investigations, we aim at providing only a broad ensemble
15 description of the processes involved rather than a detailed analysis of a single event. This
16 descriptive approach is also dictated by some of the current physical limitations of tomography
17 regarding its application to this work. Indeed, with simple geometrical considerations based on
18 the tomographic resolution (the size of the voxels) and the spacing between the network GPS
19 stations (about double the voxel size on average), one can easily recognize that there will be a
20 significant number of empty voxels, i.e. voxels without a ray crossing it. That is especially true at
21 the lower levels as rays from a given station will most probably stay within the boundaries of the
22 first altitude level voxel above it, even with a 5° elevation mask. On the first altitude level, in the
23 current geometry, about two thirds of the voxels are empty. Furthermore, at the levels just above,
24 few voxels will be traversed by rays from different stations. These limitations make for a
25 strongly undetermined problem regarding the tomography inversion and could question the
26 benefits of tomography with respect to simple IWV 2-D maps or its impact on the final water
27 vapour field compared to the a-priori values. Furthermore, in those parts of the domain where
28 there are very few GPS stations, such increased separation between stations can lead to artefacts
29 due to the IWV interpolation in an area of contrasted topography such as, for example, in the
30 south east border of our larger domain. However, when spacing between stations becomes less
31 than the voxel size, at it is the case in the central part of the COPS domain (Figure 1), these
32 restrictions are eased and the tomography inversion offers new insights into the water vapour
33 field distribution and evolution. That is also why we have focussed our analysis on a smaller
34
35
36
37
38
39
40
41
42
43
44
45
46
47
48
49
50
51
52
53
54
55
56
57
58
59
60

1
2
3
4
5
6 network with enhanced resolution whenever the meteorological situation of interest happened to
7
8 take place within the region of denser GPS station locations. Hence, the major obstacle in this
9
10 work has come from the uneven spacing between GPS stations within the network. Statistical
11
12 comparisons between a-priori and tomography water vapour fields over the entire data set have
13
14 shown that although there were little differences in those areas with few GPS stations as in the S-
15
16 E and W-N-W parts of the domain, variations up to 10% of the retrieved water vapour density
17
18 could be found in the central part of the domain where the campaign super sites were located,
19
20 surrounded by the denser part of the GPS network. Likewise, comparisons of tomography results
21
22 with 2-D IWV maps have shown that although they were globally similar, some noticeable
23
24 differences could be seen especially in the areas of marked contrasts like front boundaries and
25
26 high gradient situations as the tomography is more apt to retrieve the anisotropy of the water
27
28 vapour distribution within the denser GPS part of the domain.
29
30
31
32
33

34
35
36 The basic question we want to address in this work is the possible link that relates particular
37
38 water vapour patterns with the different types of convective initiation mechanisms and
39
40 precipitation system characteristics encountered during COPS. To do so , we have based our case
41
42 studies selection and partitioning on the general classification provided by Wulfmeyer et al.
43
44 (2011) and Kottmeir et al. (2008): 1/ High pressure air mass convection leading to locally
45
46 initiated convection; 2/ Forced wide spread convection favoured by large scale lifting and
47
48 orographic effects; 3/ Forced convection embedded in frontal or convergence zones. However,
49
50 using radar observations, we can also use the differentiation established by Hagen et al (2011)
51
52 where convection initiation takes place either 1/ on the mountain Ridges or 2/ on the Lee side of
53
54 the mountains.
55
56
57
58
59
60

1
2
3
4
5
6
7
8
9
10
11
12
13
14
15
16
17
18
19
20
21
22
23
24
25
26
27
28
29
30
31
32
33
34
35
36
37
38
39
40
41
42
43
44
45
46
47
48
49
50
51
52
53
54
55
56
57
58
59
60

IV.1. IOP 8b, 15 July 2007

This first case is certainly the most studied one among the many COPS IOPs recorded. Thus, we won't duplicate the detailed observation analyses and modelling presentations already made in Kottmeir et al. (2008), as well as in Wulfmeyer et al. (2011), Barthlott et al. (2011), Behrendt et al. (2011), and Richard et al. (2011) in this issue, and the list is certainly not exhaustive.

As shown on the radar reflectivity display of Figure 2, this event was characterized by a single isolated short lived small but very intense convective cell that developed on the eastern ridges of the Black Forest and qualifies for a "Ridge" – "High pressure air mass convection" classification. On the POLDIRAD images it is interesting to notice how the system initiates, grows, and develops through its entire life cycle with little advection, like a plume defined by a typical downstream V shape and attached to a well localized hotspot.

In Figure 3a, we show the IWV 2-D field (left column) and the horizontal water vapour density for the 1000 m height layer (right column) both for the hourly time frames from 13 to 15 UTC. Looking at these water vapour field distributions, we have to keep in mind that this might not be the best GPS analysis conditions for tomography as that area does not lie within the denser part of the GPS network, even though there is one GPS station not far away of the active cell area depicted by the black circle. Also, given that the resolution of the water vapour tomography is of the order of 16 kilometres, there is little hope to identify the hotspot where convection is activated but we can look at the larger scale evolution. In the early afternoon, a build up of humidity over the Southern Black Forest ridges is clearly visible, possibly provided by the South-Westerly flow (Wulfmeyer et al., 2011; Richard et al., 2011). However, between 13:00 UTC and 15:00 UTC, the water vapour field appears to decrease in the area where the convective cell (around 48.2°N and 8.3°E) later developed. Hence, water vapour depletion started more than

1
2
3
4
5
6 one hour before the onset of the precipitations. Comparing the tomography result to the IWV
7
8 field, it is interesting to note that tomography provide a better visual description of the local
9
10 variation of water vapour, although one must argue tat IWV is impacted by the topography and
11
12 that its relative variation with respect to a daily mean or some reference field value would also
13
14 exhibit similar build up and decrease of humidity. This fact seems to indicate that in that area,
15
16 maybe due to local forcing triggered by a localized singularity in the orography or in the ground
17
18 coverage or vegetation, there is a transfer from water vapour to liquid water. Indeed, GPS
19
20 measures water vapour content of the atmosphere but is not sensitive to liquid (or solid) water
21
22 (Solheim et al., 1999). This transfer implies the creation and/or enhancement of clouds by
23
24 generation of hydrometeors through condensation first but may be also through washing of the
25
26 lower atmosphere once the rain has started to fall. Such an effect of water vapour depletion to
27
28 support cloud formation before heavy precipitation onset had already be considered in Van
29
30 Baelen and Penide (2009) but the COPS experiment offers the first opportunity to actually
31
32 observe both the 3-D water vapour field and the precipitation system development
33
34 simultaneously. Further evidence is provided by the individual time series of IWV corresponding
35
36 to the four GPS stations surrounding the location of convective precipitation activity (Figure 3b).
37
38 Indeed, one can see the north-eastward progression of a peak of humidity within the couple of
39
40 hours before noon brought by the synoptic flow (which also cleared away a pool of humidity that
41
42 stagnated in the plain to the South-East of the Black forest in the morning). Then, by 12:00 UTC,
43
44 water vapour starts decreasing significantly, indicating the possible condensation process, while
45
46 water vapour reaches its minimum at the time the precipitation occurs.
47
48
49
50
51
52
53
54
55
56

57 *IV.2. IOP 9c, 20 July 2007*
58
59
60

1
2
3
4
5
6 This case is an example of forced convection embedded in a frontal zone characterized by high
7 water vapour densities moving ahead of the front. In the scope of this paper, it serves as a
8 support to illustrate two interesting interactions between water vapour field and precipitation
9 systems. But again, given that the GPS station density across the event analyzed is not
10 homogeneous, we will consider both IWV fields and tomography results.
11
12

13
14
15
16
17
18 First, in Figure 4, when comparing the POLDIRAD 10:00 UTC reflectivity plot with the
19 integrated water vapour distribution retrieved at the same period, one can't help noticing the
20 excellent correlation that exists between the line of active cells (the high reflectivity centres in
21 red) within the front (the area of moderate reflectivity values in green) and the areas of water
22 vapour depletion within the water vapour pattern. Those areas are highlighted by a white arc on
23 the corresponding figures and exhibit a deficit of more than 6 mm (up to 15%) of integrated
24 water vapour. Such differences are significantly larger than the recognized accuracy of GPS
25 water vapour retrievals. Hence, this point further demonstrates the possible transfer from water
26 vapour into liquid water (hydrometeors) in the areas of active convection, while further depletion
27 might be produced by aggregation of the atmospheric water vapour by the hydrometeors as they
28 drop to the ground.
29
30
31
32
33
34
35
36
37
38
39
40
41
42

43
44 Second, considering now the water vapour distribution at 10:00 UTC at the 1000 m level and the
45 POLDIRAD 10:30 UTC reflectivity map, it appears that the frontal line development is favoured
46 in those places where there exists enhanced water vapour "reservoirs". In this instance, that is
47 particularly visible for the area just east of the North-East tip of France (about 48.8° N – 8.5°E),
48 while tomography also reveals the area on the lee of the Vosges at the south end of the
49 precipitation system. Nonetheless, this figure also illustrates a current limitation with tomography
50 in those regions with few GPS stations as artefacts can appear and mask actual water vapour
51
52
53
54
55
56
57
58
59
60

signature as this is the case here over the southern Black Forest mountains. Hence, this indicates that pre-existing water vapour conditions play a dominant role in frontal development.

IV.3. IOP 9a, 18 July 2007

We selected this case because of the very localized convection spots that could be observed with POLDIRAD. Referring to the proposed classifications, this is also a case of convective activity favoured by large scale lifting due to strong flow aloft and creating isolated cells. Obviously, this is also a case of Lee side convection as all the cells observed develop on the eastern side of the Vosges. Figure 5 presents some examples of the convective and precipitation activity observed with POLDIRAD. The first one (17:00 and 17:30 UTC time frames) takes place at the exit of the Bruche valley. There, the radar reveals that the convection is triggered by a small hill within the valley exit range. Likewise, the 18:22 – 18:54 UTC cell to the south of the Vosges super-site is also triggered by a hill at the foot of the mountain range close to the exit of the Giessen valley.

In these instances and in contrast with the July 15 case studied above, the water vapour density does not build up on top of the mountain orography but it appears to cross the ridges and flow down the lee side of the Vosges into its deepest valleys. That is well indicated in Figure 6a where the water density horizontal fields at the 1000m altitude level from 14:00 to 19:00 UTC illustrate the water vapour outflow that takes place at the outcome of the Vosges mountain valleys before continuing across the Rhine valley. First (15:00 – 16:00 UTC), it is located at the exit of the Bruche valley, then, the water vapour comes across the southern lee side of the Vosges range and, in particular, around the Giessen valley (17:00 - 18:00 UTC). On Figure 6b, paying close attention to the 7.4° E zone on the constant latitude vertical cross-sections provided at 48.65°N (Bruche valley) and 48.16°N (Giessen valley), one can see the marked water vapour density reinforcement in the lowest level, while little accumulation occurs on the west side of the

1
2
3
4
5
6 mountains ranges nor on their ridges as the water vapour crosses the Vosges and spread across
7
8 the Rhine valley.
9

10 Hence, one can consider that the strong flow aloft is responsible for the water vapour crossing
11
12 over the mountain ridges and not accumulating over the mountain tops. Accordingly, the GPS
13
14 tomography retrieved water vapour fields indicate that it is the moist air descending from the
15
16 crests into the valleys that triggers the convection initiation when the flow hits a hill at the exit of
17
18 the valley which creates abrupt lifting of the low level air mass.
19
20

21
22 Furthermore, taking the opportunity of the UHF boundary layer wind profiler operation at the
23
24 nearby Vosges supersite (Figure 7), one can see that during the corresponding time period
25
26 between 16:00 and 18:00 UTC, the wind field is characterized by westerly flow aloft (above 1.5
27
28 km of altitude) but easterly, upslope winds in the lowest 500 m of the troposphere, causing low
29
30 level convergence along the Vosges lee side. Thus, we can speculate that the outgoing flow from
31
32 the valleys is meeting such upslope wind coming from the Rhine, further enhancing the lifting
33
34 effect of hills positioned near the exit of those valleys and, thus, enabling convective initiation.
35
36
37
38
39

40 *IV.4. IOP 15, 12 – 13 August 2007*

41
42 IOP 15 is of particular interest as in the course of two days three separate case studies occur.
43
44 First, there is “Ridge” convection on the 12th of August afternoon, mainly on the Vosges,
45
46 followed by a frontal passage in the Rhine valley in the early hours of the night, before “Lee
47
48 side” convection takes place on the 13th of August afternoon. Extensive work on the convective
49
50 activity observed with radars and on the role of the wind field in the convection forcing
51
52 mechanisms has already been developed in Hagen et al. (2011, this issue) and, to a lesser extend
53
54 in Bennet et al (2011, this issue) and Planche et al. (2010), so here we will keep our focus on the
55
56 water vapour fields / convective and precipitating systems interactions.
57
58
59
60

1
2
3
4
5
6 Figure 8 shows a series of radar observations of the “Ridge” event on the 12th of August.
7
8
9 POLDIRAD reveals the large scale extent of the isolated cell development over the Vosges
10
11 crests. Also, cell track origins (Hagen et al., 2011) for the entire episode show that the
12
13 convection initiation process is confined to the ridges while their relatively small extent, with
14
15 most cells decaying as they reach the Rhine valley, indicates that the advection is weak and that
16
17 there must be little moisture available over the plains to fuel the convection process. The
18
19 associated water vapour field distribution estimated with GPS tomography (Figure 9a and 9b)
20
21 further confirms that there is accumulation of water vapour from mid-morning up to early
22
23 afternoon over the Vosges Mountains to support the localized convection. In particular, the
24
25 constant latitude vertical cross-sections at 48.41°N and 48.19°N between 12:00 and 14:00 UTC
26
27 and 13:00 and 15:00 UTC respectively, passing through very active areas of the Vosges
28
29 convective zones clearly show that the water vapour does not cross the main Vosges ridge but
30
31 accumulates over the crests.
32
33
34

35
36 During the following night, there is a frontal passage with sustained precipitations that are well
37
38 documented with POLDIRAD as illustrated in Figure 10. This case can be considered as forced
39
40 convection embedded within a (cold) frontal zone. In this instance; the corresponding water
41
42 vapour field exhibits somewhat different behaviour from the previous discussions regarding the
43
44 July 15 and July 20 cases. Indeed, it appears here that the rain activity is already well established
45
46 when the system enters the COPS domain with a strong and active front brought by large scale
47
48 synoptic forcing. Hence, we have no indication regarding possible transfer of water vapour into
49
50 liquid water to support the creation and development of clouds and the precipitation onset,
51
52 associated with water vapour depletion. Instead, we notice that in the first illustration (21:00
53
54 UTC) the precipitation system contour is well correlated with a zone of high water vapour
55
56 density immediately positioned under it denoting the saturation of the atmosphere in humidity
57
58
59
60

1
2
3
4
5
6 associated with the frontal system. However, later on, high water vapour density ramifications
7
8 appear to extend ahead of the frontal system depicting possible storm outflow activities such as
9
10 those reported by Collier et al. (2008). Finally, considering the latest time frame (00:00 UTC on
11
12 13th of August), there is evidence of interaction of the orography with the development of the
13
14 frontal system as water vapour propagation is stopped by and accumulates against the foothills of
15
16 the Black Forest before rounding it by its northern tip.
17

18
19 Later in the afternoon of the 13th of August, well after the frontal passage is gone, a new episode
20
21 of isolated convection takes place but this time it happens on the Lee of the Vosges. That is
22
23 shown with the POLDIRAD observations of Figure 11, where individual cell formations can be
24
25 monitored. The reported locations of the different convection initiation spots on the lee side of
26
27 the Vosges (almost exclusively) and the corresponding duration of the cell tracks extending well
28
29 across the Rhine valley offer a quite different pattern from the 12th of August situation (see
30
31 Hagen et al., 2011 for further details). Considering now the corresponding water vapour density
32
33 fields, the horizontal distribution at the 1000 m level, shown in Figure 12a, indicates no specific
34
35 accumulation towards the mountain ridges but relatively high water vapour values in the Rhine
36
37 valley instead and reinforcement of the water vapour density at the foothill of the Vosges in
38
39 those areas and times when convection seen with POLDIRAD happen. That is the case at 12:00
40
41 and 13:00 UTC along the North-East side of the Vosges orography. Furthermore, by 15:00 and
42
43 16:00 UTC, there is a marked increase of water vapour at the exit of one of the central Vosges
44
45 mountain valleys, associated with the generation of a strong cell identified in the South of the
46
47 POLDIRAD field of view at 16:30. To better illustrate these findings, Figure 12b shows two
48
49 series of vertical cross sections at constant latitude. The first one at 48.19°N spans the time range
50
51 from 12:00 to 14:00 UTC and passes through the cells observed on the North of the Vosges
52
53 mountain range. Besides, high values of water vapour in the Rhine valley and along the western
54
55
56
57
58
59
60

1
2
3
4
5
6 slopes of the Black Forest, it shows a local burst of water vapour at the foot of the Vosges
7
8 Mountains at 13:00 UTC, corresponding to the precipitation cells monitored. Likewise, the
9
10 second series of vertical cross sections at constant latitude 48.41°N spans the time range from
11
12 15:00 to 17:00 UTC and passes through the cell observed in the southern domain of POLDIRAD
13
14 in Figure 11. In this case, the strong water vapour outflow associated with the convective cell
15
16 initiation corresponds to water vapour advection above the mountain ridge onto the lee side
17
18 down along mountain valley. Also quite interesting is Figure 12c, where we present the vertical
19
20 cross sections at constant longitude spanning the time range from 11:00 to 16:00 UTC and
21
22 passing along the Vosges front ranges. Looking at the first three time frames (11:00 to 13:00
23
24 UTC), we find a strong evidence of water vapour convergence at the location of a small hill by
25
26 about 48.5°N where the strong cell visible at 13:00 with POLDIRAD develops. Indeed, from
27
28 11:00 to 12:00, water vapour levels increase significantly on both sides of the central hill but by
29
30 13:00, water vapour has now converged on that hill where convective initiation takes place.
31
32 Later, the strong outflow leading to the large convective cell initiation in the south of
33
34 POLDIRAD field of view is also well identified with a major increase of water vapour density
35
36 over the first levels of the atmosphere around the 48°N latitude.
37
38
39
40
41
42
43
44

V/ Concluding remarks and future work

45
46
47
48
49
50 In this work, we have considered the water vapour field evolution with respect to the various
51
52 precipitation and convective initiation situations monitored during the COPS campaign. Hence,
53
54 we have tried to gain new insights on the role of water vapour in the precipitation systems
55
56 lifecycle. To do so, we have looked at the water vapour field patterns and behaviour as a function
57
58
59
60

1
2
3
4
5
6 of orography dependant convective initiation, i.e. Ridge or Lee side convection, as well as a
7
8 function of background synoptic conditions for larger scale systems.
9

10
11
12
13 First, for ridge convection, it is necessary to get significant water vapour accumulation over the
14
15 crests of the mountains as a precursor to convection onset. That implies that the synoptic wind is
16
17 not too important such that it does not carry the water vapour across the range, or that local
18
19 conditions or singular orographic features favour water vapour blocking and accumulation over
20
21 the crest. Then, the water vapour acts as a fuel for the convective initiation or regeneration over
22
23 the mountain ridge. On the opposite, when the water vapour does not stagnate over the
24
25 mountains but passes the ridge to flow down the main orography, the corresponding valley flows
26
27 are prone to generate lee side convection when they encounter a small hill and/or some
28
29 converging flow coming from the warmer plains in the lowest layers of the atmosphere. This
30
31 combined effect probably creates a significant lifting of high water vapour air and triggers
32
33 convection.
34
35
36
37

38
39 Second, we have noticed an interesting feature where water vapour seemed to decrease
40
41 singularly some times before the actual onset of precipitation or precipitation reinforcement. One
42
43 hypothesis is that water vapour has been transformed into liquid water through the condensation
44
45 processes that occur within the convection, meaning that water vapour has given way to cloud
46
47 formation. Of course, this needs further detail studies with more measurements in order to
48
49 confirm the hypothesis.
50
51

52
53 Finally, we have also noted contrasted behaviour of the water vapour field with respect to large
54
55 scale precipitation systems. When this is a large and established synoptic scale frontal passage,
56
57 the water vapour field appears in phase with the frontal system: the maximum water vapour lies
58
59 under the front where the air is saturated by rain. However, in the case of low intensity
60

1
2
3
4
5
6 precipitation front, water vapour depletion appeared in those spots where the convective cells
7 developed, imbedded in the larger system. That seems to indicate that the cell actually feed on
8 the underlying water vapour. That assumption is further confirmed by the fact that the convective
9 front “trails” the water vapour field and develops preferably in those areas where the water
10 vapour densities are the highest.
11
12
13
14
15
16

17
18
19
20 At this stage, the work performed here has been essentially qualitative but we feel that it has
21 proven useful in pointing out to very interesting mechanisms that link water vapour field
22 distribution and evolution with respect to the precipitating system dynamics and behaviour.
23
24
25
26 Nonetheless, these hypotheses need to be further addressed to draw on definite conclusions. That
27 is the object of currently ongoing studies.
28
29
30
31
32

33
34 Another aspect of this work has also been to test GPS tomography for water vapour field
35 retrieval using only the GPS and surface data. The restitutions obtained are quite reasonable and
36 allows meaningful interpretations, in particular in the part of the domain where the GPS station
37 density is the highest where we could retrieve higher resolution of the water vapour density field.
38
39
40
41 However, by using only GPS data, the vertical structure of the water vapour field is somewhat
42 reduced unless GPS stations are close enough to form a dense network where multiple rays can
43 cross in individual voxels. Hence, now that we are confident in the GPS tomography method to
44 retrieve 3-D water vapour fields, we plan to improve the current analysis scheme by enhancing
45 the algorithm such that measured profiles of water vapour density within the COPS domain can
46 be accounted for during the inversion initialisation step. That should prove useful in order to
47 render more vertical structures in the tomographic results and avoid the vertical dilution of the
48
49
50
51
52
53
54
55
56
57
58
59
60
61
62
63
64
65
66
67
68
69
70
71
72
73
74
75
76
77
78
79
80
81
82
83
84
85
86
87
88
89
90
91
92
93
94
95
96
97
98
99
100
101
102
103
104
105
106
107
108
109
110
111
112
113
114
115
116
117
118
119
120
121
122
123
124
125
126
127
128
129
130
131
132
133
134
135
136
137
138
139
140
141
142
143
144
145
146
147
148
149
150
151
152
153
154
155
156
157
158
159
160
161
162
163
164
165
166
167
168
169
170
171
172
173
174
175
176
177
178
179
180
181
182
183
184
185
186
187
188
189
190
191
192
193
194
195
196
197
198
199
200
201
202
203
204
205
206
207
208
209
210
211
212
213
214
215
216
217
218
219
220
221
222
223
224
225
226
227
228
229
230
231
232
233
234
235
236
237
238
239
240
241
242
243
244
245
246
247
248
249
250
251
252
253
254
255
256
257
258
259
260
261
262
263
264
265
266
267
268
269
270
271
272
273
274
275
276
277
278
279
280
281
282
283
284
285
286
287
288
289
290
291
292
293
294
295
296
297
298
299
300
301
302
303
304
305
306
307
308
309
310
311
312
313
314
315
316
317
318
319
320
321
322
323
324
325
326
327
328
329
330
331
332
333
334
335
336
337
338
339
340
341
342
343
344
345
346
347
348
349
350
351
352
353
354
355
356
357
358
359
360
361
362
363
364
365
366
367
368
369
370
371
372
373
374
375
376
377
378
379
380
381
382
383
384
385
386
387
388
389
390
391
392
393
394
395
396
397
398
399
400
401
402
403
404
405
406
407
408
409
410
411
412
413
414
415
416
417
418
419
420
421
422
423
424
425
426
427
428
429
430
431
432
433
434
435
436
437
438
439
440
441
442
443
444
445
446
447
448
449
450
451
452
453
454
455
456
457
458
459
460
461
462
463
464
465
466
467
468
469
470
471
472
473
474
475
476
477
478
479
480
481
482
483
484
485
486
487
488
489
490
491
492
493
494
495
496
497
498
499
500
501
502
503
504
505
506
507
508
509
510
511
512
513
514
515
516
517
518
519
520
521
522
523
524
525
526
527
528
529
530
531
532
533
534
535
536
537
538
539
540
541
542
543
544
545
546
547
548
549
550
551
552
553
554
555
556
557
558
559
560
561
562
563
564
565
566
567
568
569
570
571
572
573
574
575
576
577
578
579
580
581
582
583
584
585
586
587
588
589
590
591
592
593
594
595
596
597
598
599
600
601
602
603
604
605
606
607
608
609
610
611
612
613
614
615
616
617
618
619
620
621
622
623
624
625
626
627
628
629
630
631
632
633
634
635
636
637
638
639
640
641
642
643
644
645
646
647
648
649
650
651
652
653
654
655
656
657
658
659
660
661
662
663
664
665
666
667
668
669
670
671
672
673
674
675
676
677
678
679
680
681
682
683
684
685
686
687
688
689
690
691
692
693
694
695
696
697
698
699
700
701
702
703
704
705
706
707
708
709
710
711
712
713
714
715
716
717
718
719
720
721
722
723
724
725
726
727
728
729
730
731
732
733
734
735
736
737
738
739
740
741
742
743
744
745
746
747
748
749
750
751
752
753
754
755
756
757
758
759
760
761
762
763
764
765
766
767
768
769
770
771
772
773
774
775
776
777
778
779
780
781
782
783
784
785
786
787
788
789
790
791
792
793
794
795
796
797
798
799
800
801
802
803
804
805
806
807
808
809
810
811
812
813
814
815
816
817
818
819
820
821
822
823
824
825
826
827
828
829
830
831
832
833
834
835
836
837
838
839
840
841
842
843
844
845
846
847
848
849
850
851
852
853
854
855
856
857
858
859
860
861
862
863
864
865
866
867
868
869
870
871
872
873
874
875
876
877
878
879
880
881
882
883
884
885
886
887
888
889
890
891
892
893
894
895
896
897
898
899
900
901
902
903
904
905
906
907
908
909
910
911
912
913
914
915
916
917
918
919
920
921
922
923
924
925
926
927
928
929
930
931
932
933
934
935
936
937
938
939
940
941
942
943
944
945
946
947
948
949
950
951
952
953
954
955
956
957
958
959
960
961
962
963
964
965
966
967
968
969
970
971
972
973
974
975
976
977
978
979
980
981
982
983
984
985
986
987
988
989
990
991
992
993
994
995
996
997
998
999
1000

1
2
3
4
5
6
7
8
9 Furthermore, we plan to reprocess the periods of interest with higher resolution both in space
10 (especially in the vertical for levels where multiple rays can cross within individual voxels) and
11 time (down to 20 minutes) in order to refine our comparisons with the radar observations in the
12 core of the COPS domain where the GPS station network is sufficiently dense. This will allow us
13 to further study some these events where we can relate the convective initiation to fine
14 orographic features such as hills within the exit of mountain valleys.
15
16
17
18
19
20
21
22
23

24 Finally, we will also increase the scope of the present analyses by using other means of
25 observations and supporting atmospheric variables, such as the low level wind from dual
26 Doppler radar analysis as well as VERA analysis, ground based and airborne lidar
27 measurements, etc.. Likewise, we will compare our measurements and field retrievals with
28 model outputs as a way to both validate the corresponding results and to investigate in detail the
29 processes and controlling factors of the precipitation systems lifecycle.
30
31
32
33
34
35
36
37
38
39
40
41
42

43 *Acknowledgements*

44
45
46
47
48
49
50
51
52
53
54
55
56
57
58
59
60

The lead author would like to thank the anonymous reviewers for their precise and constructive comments and, in particular, for a series of thought provoking questions and suggestions which, without a doubt, have significantly contributed to the improvement of the article while they have also initiated further investigations in progress.

The COPS campaign implementation and the instrument participation (radars and GPS in this instance) were made possible through the financial support of the DFG Priority Programme 1167

1
2
3
4
5
6 in Germany, and ANR (grant ANR-06-BLAN-0018-04: COPS/France) and CNRS/INSU
7
8 (LEFE/IDAO program) in France.
9
10
11
12
13
14
15
16
17
18
19
20
21
22
23
24
25
26
27
28
29
30
31
32
33
34
35
36
37
38
39
40
41
42
43
44
45
46
47
48
49
50
51
52
53
54
55
56
57
58
59
60

For Peer Review

REFERENCES

Barthlott C, Richard E, Burton R, Gadian A, Blyth AM, Mobbs S, Bauer H-S, Schwitalla T, Keil C, Trentmann J, Kern B, Seity Y, Kirshbaum D, Hanley K, Handwerker J. 2011. Initiation of deep convection at marginal instability in an ensemble of mesoscale models: A case study from COPS. *Quart. J. Roy. Meteor. Soc.*, this special issue.

Behrendt A, et al. 2011. The impact of the spatiotemporal variability of water vapour on convection initiation in low mountains: Multi-sensor observations during COPS IOP8b; *Quart. J. Roy. Meteor. Soc.*, this special issue.

Bender, M., Dick, G., Wickert, J., Schmidt, T., Song, S., Gendt, G., Ge, M., and Rothacher, M., 2008: Validation of GPS slant delays using water vapour radiometers and weather models. *Meteorologische Zeitschrift*, **17**(6), 807-812.

Bennett, L. J., A.M. Blyth, R.M. Burton, A. Gadian, T.M. Weckwerth, A. Behrendt, P. Di Girolamo, M. Dorninger, S.-J. Lock, V.H. Smith, and S.D. Mobbs, 2011: Initiation of convection over the Black Forest mountains during COPS IOP15a, *Quart. J. Roy. Meteor. Soc.*, this special issue.

Bevis M., S. Businger, T. A. Herring, C. Rocken, R. A. Anthes, and R. H. Ware, 1992: GPS Meteorology: Remote sensing of atmospheric water vapour using the Global Positioning System; *Journal Geophys. Res.*, **103**, 15787-15801.

1
2
3
4
5
6 Bevis M., S. Businger, S. Chiswell, T. A. Herring, R. A. Anthes, C. Rocken, and R. H. Ware,
7
8 1994: GPS Meteorology: Mapping zenith wet delay onto precipitable water; *Journal of Applied*
9
10 *Meteorology*, 33, 379-386.
11
12

13
14
15 Boehm, J., Niell, A., Tregoning, P., and Schuh, H., 2006: Global Mapping Function (GMF): A
16
17 new empirical mapping function based on numerical weather model data. *Geophysical Research*
18
19 *Letters*, 33:L07304.
20
21

22
23
24 Braun, J., C. Rocken and J. Liljegren, 2003: Comparisons of Line-of-Sight Water Vapour
25
26 Observations Using the Global Positioning System and a Pointing Microwave Radiometer, *J. of*
27
28 *Atmosph. Ocean Techn.*, 20, 606-612.
29
30

31
32
33 Businger S., S.R. Chiswell, M. Bevis, J. Duan, R.A. Anthes, C. Rocken, R.H. Ware, M. Exner,
34
35 T. VanHove, and F. Solheim, 1996: The promise of GPS in atmospheric monitoring; *Bull. Amer.*
36
37 *Meteor. Soc.*, 77, 5-18.
38
39

40
41 Champollion, C., C. Flamant, O. Bock, F. Masson, D.D. Turner, T. Weckwerth, 2009: Mesoscale
42
43 GPS tomography applied to the 12 June 2002 convective initiation event of IHOP_2002;
44
45 *Quarterly Journal of the Royal Meteorological Society*, 135, p 645–662; DOI: 10.1002/qj.386.
46

47
48 Champolion, C., F. Masson, M-N Bouin, A. Walpersdorf, E. Doerflinger, O. Bock, J. Van
49
50 Baelen, 2005 : GPS water vapour tomography : First results from the ESCOMPTE field
51
52 experiment, *Atmospheric Research*, 74, 253-274.
53

54
55 Collier, C., F. Davies, J. Davis, G. Pearson, and M. Hagen, 2008: Doppler radar and lidar
56
57 observations of a thunderstorm outflow, *Proceedings of the fifth European Conference on radar*
58
59 *in Meteorology and Hydrology*, Helsinki, Finland, 30 June - 4 July 2008.
60

1
2
3
4
5
6 Duan J. M. Bevis, P. Fang, Y. Bock, S. Chiswell, S. businger, C. Rocken , F. Solheim, T.
7 VanHove, R. Ware, S. McClusky, T.A. Herring, and R.W. King, 1996: GPS meteorology: direct
8 estimation of the absolute value of precipitable water; *J. Appl. Meteor.*, **35**, 830-838.
9

10
11
12
13 Emardson, T. R., and H. J. P. Derks, 1999: On the relation between the wet delay and the
14 integrated precipitable water vapour in the European atmosphere; *Meteorological Applications*,
15 **6**, 1-12.
16
17

18
19
20 Flores, A., A. Rius, and G. Ruffini, 2000: 4D tropospheric tomography using GPS slant wet
21 delays, *Ann. Geophys.*, **18**, 223-224.
22
23

24
25 Flores A., J. Vilà-Guerau de Arellano, L. Gradinarsky, and A. Rius, 2001: Tomography of the Lower
26 Troposphere Using a Small Dense Network of GPS Receivers, *IEEE Transactions on*
27 *Geoscience and Remote Sensing*, **39** (2), 439-447.
28
29

30
31
32 Gendt, G., Dick, G., Reigber, C., Tomassini, M., Liu, Y., and Ramatschi, M., 2004: Near real
33 time GPS water vapour monitoring for numerical weather prediction in Germany. *Journal of the*
34 *Meteorological Society of Japan*, **82**(1B):361–370.
35
36
37

38
39
40
41 Gendt, G., Dick, G., Rius, A., and Sedo, P., 2001: Comparison of software and techniques for
42 water vapour estimation using german near real-time GPS data. *Physics and Chemistry of the*
43 *Earth (A)*, **26**(6-8):417–420.
44
45
46
47

48
49
50 Gradinarsky L.P., and Jarlemark P., 2004: Ground based GPS tomography of water vapour:
51 analysis of simulated and real data; *Journal of the Meteorological society of Japan*, **82**(1B), 551-
52 560.
53
54
55
56
57
58
59
60

1
2
3
4
5
6
7 Ha, S-Y., Y.-H Kuo and Y.-R, Guo, 2003: Variational Assimilation of Slant-Path Wet Delay
8
9 Measurements from a Hypothetical Ground-Based GPS Network. Part I: Comparison with
10
11 Precipitable Water Assimilation, *Mon. Wea. Rev.*, **131**, 2635-2655.
12

13
14
15 Hagen, M., J. van Baelen, E. Richard, 2011 : Influence of the Wind Profile on the Initiation of
16
17 Convection in Mountainous Terrain ; *Quart. J. Roy. Meteor. Soc.*, this special issue.
18

19
20
21
22 Kottmeier, Ch., N. Kalthoff, Ch. Barthlott, U. Corsmeier, J. Van Baelen, A. Behrendt, R.
23
24 Behrendt, A. Blyth, R. Coulter, S. Crewell, P. Di Giromalo, M. Dorninger, C. Flamant, Th.
25
26 Foken, M. Hagen, C. Hauck, H. Höller, H. Konow, M. Kunz, H. Mahlke, S. Mobbs, E. Richard,
27
28 R. Steinacker, T. Weckwerth, A. Wieser, and V. Wulfmeyer, 2008: Mechanisms initiating deep
29
30 convection over complex terrain during COPS. *Meteorol. Z.*, **17**, 931-948.
31
32
33

34
35
36
37 Liljegren J.C., B.M. Lesht, T. VanHove, and C. Rocken, 1999, "A comparison of integrated water
38
39 vapor from microwave radiometer, balloon-borne sounding system, and global positionng
40
41 system", *Ninth ARM Science Team Meeting*, San Antonio, TX, March 22-26, 1999.
42

43
44
45 Liu, H., and M. Xue, 2006: Retrieval of Moisture from Slant-Path Water Vapour Observations of
46
47 a Hypothetical GPS Network Using a Three-Dimensional Variational Scheme with Anisotropic
48
49 Background Error, *Mon. Wea. Rev.*, **134**, 933-949.
50

51
52
53
54 MacDonald, A., Y. Xie and R. Ware, 2002: Diagnosis of Three Dimensional Water Vapour
55
56 Using Slant Observations from a GPS Network, *Mon. Wea. Rev.*, **130**, 386-397.
57
58
59
60

1
2
3
4
5
6 McClatchey, R. A., R. W. Fenn, J.E.A. Selby, F. E. Volz, and J. S. Garing, 1972: Optical
7
8 properties of the atmosphere, AFCRL-72-0497, 108 pp.
9

10
11
12
13 Menke W., 1989: Geophysical Data Analysis: Discrete Inverse Theory; *Academic Press*,
14
15 London, United Kingdom.
16

17
18
19
20 Niell, A. E., 1996: Global mapping functions for the atmosphere delay at radio wavelengths,
21
22 *Journal of Geophysical Research*, **101**(B2):3227–3246.
23
24

25
26
27 Planche C, Wobrock W, Flossmann AI, Tridon F, Van Baelen J, Pointin Y, Hagen M., 2010 :
28
29 The influence of aerosol particle number and hygroscopicity on the evolution of convective
30
31 cloud systems and their precipitation: A numerical study based on the COPS observations on 12
32
33 August 2007. *Atmos. Res.* In press. DOI: 10.1016/j.atmosres.2010.05.003.
34
35

36
37
38 Reverdy, M., 2008: Estimation des paramètres atmosphériques par GPS: analyse de la variabilité
39
40 spatio-temporelle de la vapeur d'eau, Thesis of the Université Blaise Pascal, Clermont-Ferrand,
41
42 France, n°598, 264pp.
43
44

45
46
47
48 Reverdy, M, Van Baelen J, Walpersdorf A, Dick G, Hagen M, Richard E. 2009: Water vapour
49
50 fields retrieval with tomography software. *Ann. Meteorol.* **44**: Deutscher Wetterdienst,
51
52 Offenbach. ISBN 978-3-88148-440-4, 144-145. www.pa.op.dlr.de/icam2009/extabs
53
54

55
56
57 Richard, E., C. Flamant, F. Bouttier, J. Van Baelen, C. Champollion, M. Hagen, J. Cuesta, P.
58
59 Bosser, G. Pigeon, S. Argence, J. Arnault, P. Brousseau, Y. Seity, J.-P. Chaboureau, P.
60

1
2
3
4
5
6 Limnaios, F. Masson, Y. Pointin, P. Di Girolamo, V. Wulfmeyer, 2009 : La campagne COPS :
7
8 Initiation et cycle de vie de la convection en région montagneuse, *La Météorologie*, **64**, 32-42.
9

10
11
12
13 Richard E, Chaboureau J-P, Flamant C, Champollion C, Hagen M, Schmidt K, Kiemle C,
14
15 Corsmeier C, Barthlott C., 2011: Forecasting Summer convection over the Black Forest: a case
16
17 study from the COPS experiment. *Quart. J. Roy. Meteor. Soc.*, this special issue.
18

19
20
21
22 Schroth, A.C., M.S. Chandra, and P.F. Mesichner, 1988: A C-Band Coherent Polarimetric Radar
23
24 for Propagation and Cloud Physics Research. *J. Atmos. Ocean. Technol.*, **5**, 803–822.
25

26
27
28
29 Saastamoinen, J., 1972: Atmospheric correction for the troposphere and stratosphere in radio
30
31 ranging of satellites; *The use of Artificial Satellites for Geodesy*, **15**, *Geophysical Monograph*,
32
33 247-251, Amer. Geophys. Union, Washington D.C., USA.
34

35
36
37
38 Solheim, F., J. Vivekanandan, R. Ware and C. Rocken, 1999: Propagation Delays Induced in
39
40 GPS Signals by Dry Air, Water Vapour, Hydrometeors and other Atmospheric Particulates, *J.*
41
42 *Geophys Res.*, **104** (D8), 9663-9670.
43

44
45
46
47 Steinacker, R., M. Ratheiser, B. Bica, B. Chimani, M. Dorninger, W. Gepp, C. Lotteraner, S.
48
49 Schneider, and S. Tschannett, 2006: A Mesoscale Data Analysis and Downscaling Method over
50
51 Complex Terrain. *Mon. Wea. Rev.*, **134**, 2758–2771.
52

53
54
55
56 Tarantola A., 2005: Inverse Problem Theory and methods for model parameter estimation,
57
58 *Society for industrial and applied mathematics*, Philadelphia, USA.
59
60

1
2
3
4
5
6
7
8
9 Tregoning P., R. Boers, D. O'Brien, and M. Hendy, 1998: Accuracy of absolute precipitable
10 water vapour estimates from GPS observations; *J. Geophys. Res.*, **103**, 28701-28710.
11
12

13
14
15 Van Baelen, J., J-P Aubagnac, A. Dabas, 2005 : Comparison of near real-time estimates of
16 integrated water vapour derived with GPS, radiosondes, and microwave radiometer, *J. of*
17 *Atmosph. Ocean Techn.*, **22**, 201-210.
18
19
20
21
22

23
24
25 Van Baelen, J., and G. Penide, 2009 : Study of water vapour vertical variability and possible
26 cloud formation with a small network of GPS stations, *Geophys. Res. Lett.*, **36**, L02804,
27 doi:10.1029/2008GL036148.
28
29
30
31

32
33
34 Wang J., L. Zhang, A. Dai, T. Van Hove, J. Van Baelen, 2007 : A near-global 2-hourly data set
35 of atmospheric precipitable water from ground-based GPS measurements, *J. of Geophys. Res.*,
36 2007, 112D11D11107.
37
38
39
40
41

42
43 Ware, R., C. Alber, C. Rocken and F. Solheim, 1997: Sensing integrated water vapour along
44 GPS ray paths, *Geophys. Res. Lett.*, **24**, 417-420.
45
46
47
48
49

50 Wulfmeyer, V., A. Behrendt, H.S. Bauer, C. Kottmeier, U. Corsmeier, A. Blyth, G. Craig, U.
51 Schumann, M. Hagen, S. Crewell, P. Di Girolamo, C. Flamant, M. Miller, A. Montani, S.
52 Mobbs, E. Richard, M.W. Rotach, M. Arpagaus, H. Russchenberg, P. Schlüssel, M. König, V.
53 Gärtner, R. Steinacker, M. Dorninger, D.D. Turner, T. Weckwerth, A. Hense, and C. Simmer,
54
55
56
57
58
59
60

1
2
3
4
5
6 2008: RESEARCH CAMPAIGN: The Convective and Orographically Induced Precipitation
7
8 Study. *Bull. Amer. Meteor. Soc.*, **89**, 1477–1486.
9

10
11
12
13 Wulfmeyer V, Behrendt A, Kottmeier C, Corsmeier U, Barthlott C, Craig G, Hagen M,
14 Althausen D, Aoshima, F, Arpagaus M, Bauer HS, van Baelen J, Bennett, L, Blyth A, Brandau
15 C, Champollion C, Crewell S, Dick G, Dorninger M, Dufournet Y, Eigenmann R, Engelmann R,
16 Flamant C, Foken T, Di Girolamo P, Groenemeijer P, Gorgas T, Grzeschik M, Peters G,
17 Handwerker J, Hauck C, Höller H, Junkermann W, Kalthoff N, Kiemle C, König M, Krauss L,
18 Long C, Madonna F, Mobbs S, Neininger B, Pal S, Pigeon G, Richard E, Rotach MW,
19 Russchenberg H, Schwitalla, T, Smith V, Steinacker R, Trentmann J, Turner DD, Vogt S,
20 Volkert H, Weckwerth T, Wernli H, Wieser, A., 2011: The Convective and Orographically
21 Induced Precipitation Study (COPS): The scientific strategy, the field phase, and first highlights.
22 *Quart. J. Roy. Meteor. Soc.*, this special issue.
23
24
25
26
27
28
29
30
31
32
33
34
35
36
37

38 Zumberge, J. F., Heflin, M. B., Jefferson, D. C., Watkins, M. M., and Webb, F. H., 1997: Precise
39 point positioning for the efficient and robust analysis of GPS data from large networks, *Journal*
40 *of Geophysical Research*, **102**(B3):5005–5018.
41
42
43
44
45
46
47
48
49
50
51
52
53
54
55
56
57
58
59
60

Figure Captions:

Figure 1: The COPS campaign domain with the GPS stations network (white dots), the POLDIRAD (P) weather radar location (white diamond) with its 120 km radius field of view circle, and the instrumentation supersites (white squares) with, from West to East, the Vosges low mountain site (V), the Rhine valley site (R), the Hornisgrinde mountain site (H), the Murg valley site (M), and the Deckenpfronn site near Stuttgart (S). The main orographic features are also indicated: the Vosges Mountains to the West, the Rhine Valley in the centre, and the Black Forest Mountains to the East.

Figure 2: POLDIRAD reflectivity PPI observations of the heavy precipitation isolated cell on July 15, 2007 (IOP 8b) at 14:20, 14:40, 15:00, and 15:20 UTC, respectively. The colour scale indicates the reflectivity from -10 to 60 DBz.

Figure 3a : GPS IWV 2-D fields (left column) and tomography horizontal water vapour density fields at the 1000 m height layer (right column) from 13:00 to 15:00 UTC on July 15, 2007 (IOP 8b). The IWV scale goes from 5 to 40 mm and the water vapour density scale goes from 4 to 14 g/m³. The black circle indicates the area of convective activity seen on the radar display of Figure 2.

Figure 3b: IWV time series for July 15, 2007 (IOP 8b: Day 196) for the four surrounding GPS stations around the area of convective activity at 15:00 UTC in the Black Forest (black circle on the previous figure). Positions on the plots correspond to the relative cardinal positions of the GPS stations.

1
2
3
4
5
6 Figure 4: POLDIRAD reflectivity PPI observations on July 20, 2007 (IOP 9c) at 10:00, and
7
8 10:30 UTC, respectively (left column) and GPS IWV field (top right panel) and
9
10 tomography horizontal water vapour density field for the 1000 m (bottom right
11
12 panel) height layer at 10:00 UTC on July 20, 2007 (IOP 9c). The radar reflectivity
13
14 scale goes from -10 to 60 DBz. The IWV scale goes from 17 to 42 mm and the
15
16 water vapour density scale goes from 6 to 16 g/m³.
17
18
19
20
21

22 Figure 5: POLDIRAD reflectivity PPI observations on July 18, 2007 (IOP 9a) at 17:00,
23
24 17:30, 18:22, and 18:54 UTC, respectively. The colour scale indicates the
25
26 reflectivity from -10 to 60 DBz.
27
28
29

30 Figure 6a: GPS tomography horizontal water vapour density fields for the 1000 m height layer
31
32 from 14:00 to 19:00 UTC, on July 18, 2007 (IOP 9a). The water vapour density
33
34 scale goes from 4 to 14 g/m³. The Bruche and Giessen valleys are indicated.
35
36
37
38

39 Figure 6b: GPS tomography vertical water vapour density cross-sections at constant latitude
40
41 48.64° N (left column) and 48.19° N (right column) from 15:00 to 17:00 and 16:00
42
43 to 18:00 UTC, respectively, on July 18, 2007 (IOP 9a). The water vapour density
44
45 scale goes from 6 to 14 g/m³.
46
47
48
49

50 Figure 7: Supersite Vosges UHF wind profiler time/height plot for July 18, 2007 (IOP 9a).
51
52 Colour scale indicates wind amplitude in m/s while arrows indicate wind direction.
53
54
55
56
57
58
59
60

1
2
3
4
5
6
7 Figure 8: POLDIRAD reflectivity PPI observations on August 12, 2007 (IOP 15a) at 12:20,
8 13:20, 14:20 and 15:20 UTC, respectively. The colour scale indicates the
9 reflectivity from -10 to 60 DBz.
10
11
12

13
14
15 Figure 9a: GPS tomography horizontal water vapour density fields for the 1000 m height layer
16 for the 9:00, 11:00, 13:00, and 15:00 UTC time frames, respectively, on August 12,
17 2007 (IOP 15a). The water vapour density scale goes from 4 to 14 g/m³. The dash
18 lines indicate the vertical cross-sections of Figure 9b.
19
20
21
22
23

24
25
26 Figure 9b: GPS tomography vertical water vapour density cross-sections at constant latitude
27 48.41° N (left column) and 48.19° N (right column) from 12:00 to 14:00 and 13:00
28 to 15:00 UTC, respectively, on August 12, 2007 (IOP 15a). The water vapour
29 density scale goes from 5 to 11 g/m³.
30
31
32
33
34
35
36
37

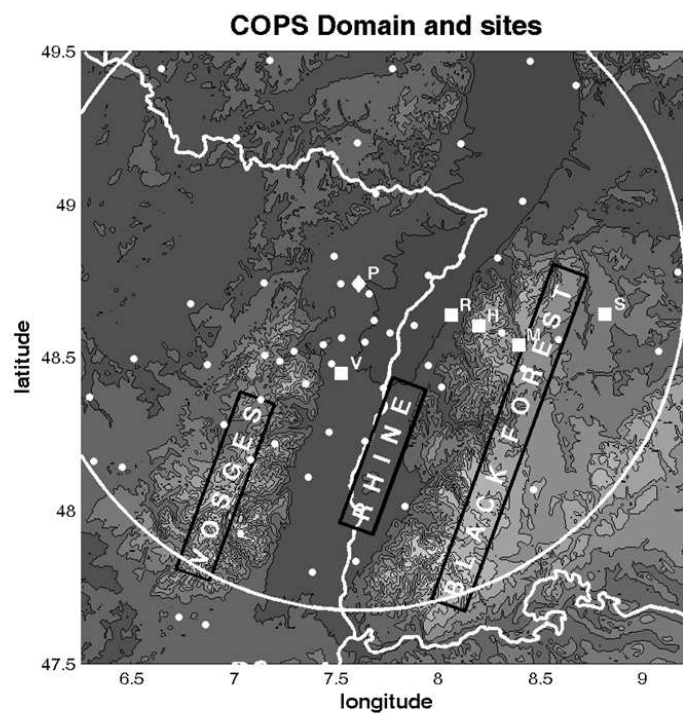
38 Figure 10: POLDIRAD reflectivity PPI observations on August 12, 2007 at 21:00, 22:00,
39 23:00, and August 13, 2007 at 00:00 UTC (IOP 15) respectively (left column) and
40 GPS tomography horizontal water vapour density fields at the 1000 m height layer
41 for the same times (right column). The radar reflectivity scale goes from -10 to 60
42 DBz. The water vapour density scale goes from 3 to 13 g/m³.
43
44
45
46
47
48
49
50

51
52 Figure 11: POLDIRAD reflectivity PPI observations of isolated cells on August 13, 2007 (IOP
53 15b) at 13:00, 14:10, 15:21, and 16:30 UTC, respectively. The colour scale
54 indicates the reflectivity from -10 to 60 DBz.
55
56
57
58
59
60

1
2
3
4
5
6 Figure 12a : GPS tomography horizontal water vapour density cuts for the 1000 m height layer
7
8 from 11:00 to 16:00 UTC, on August 13, 2007 (IOP 15b). The water vapour density
9
10 scale goes from 3 to 13 g/m³. The dash lines indicate the vertical cross-sections of
11
12 Figure 12b and 12c.
13
14
15
16
17

18 Figure 12b : GPS tomography vertical water vapour density cross-sections at constant latitude
19
20 48.41° N (left column) and 48.19° N (right column) from 12:00 to 14:00 and 15:00
21
22 to 17:00 UTC, respectively, on August 13, 2007 (IOP 15b). The water vapour
23
24 density scale goes from 5 to 11 g/m³.
25
26
27
28

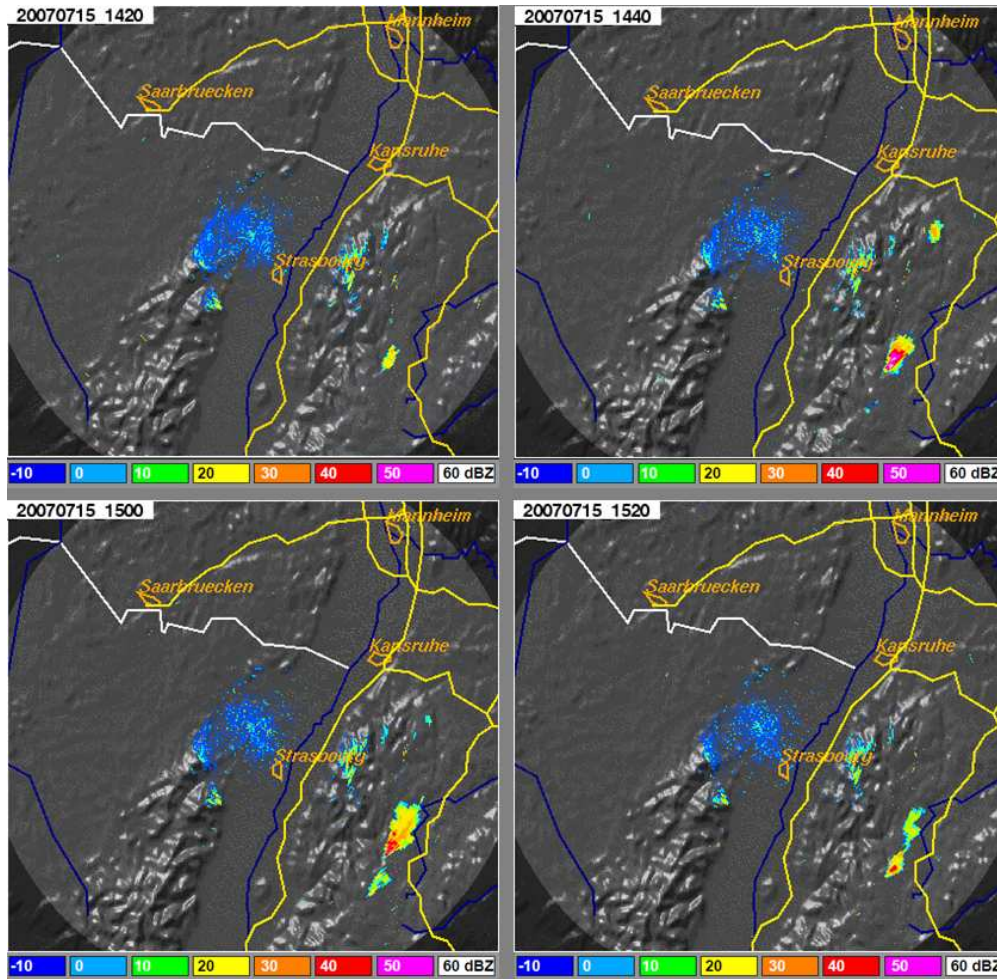
29 Figure 12c : GPS tomography vertical water vapour density cross-sections at constant longitude
30
31 7.34° E from 11:00 to 16:00 UTC, on August 13, 2007 (IOP 15b). The water vapour
32
33 density scale goes from 5 to 11 g/m³.
34
35
36
37
38
39
40
41
42
43
44
45
46
47
48
49
50
51
52
53
54
55
56
57
58
59
60



32 The COPS campaign domain with the GPS stations network (white dots), the POLDIRAD (P) weather
33 radar location (white diamond) with its 120 km radius field of view circle, and the instrumentation
34 supersites (white squares) with, from West to East, the Vosges low mountain site (V), the Rhine
35 valley site (R), the Hornisgrinde mountain site (H), the Murg valley site (M), and the Deckenfronn
36 site near Stuttgart (S). The main orographic features are also indicated: the Vosges Mountains to
37 the West, the Rhine Valley in the centre, and the Black Forest Mountains to the East.

38
39
40
41
42
43
44
45
46
47
48
49
50
51
52
53
54
55
56
57
58
59
60

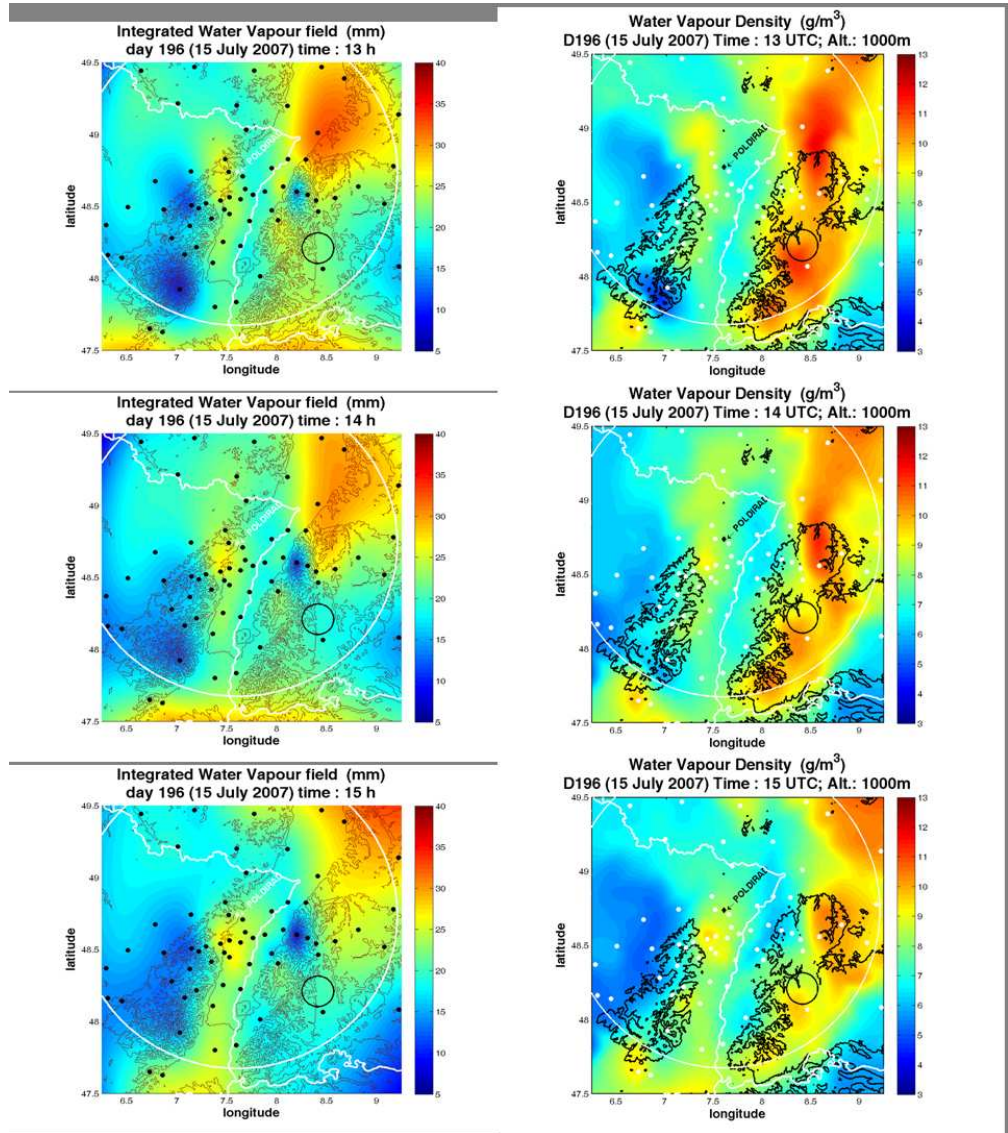
1
2
3
4
5
6
7
8
9
10
11
12
13
14
15
16
17
18
19
20
21
22
23
24
25
26
27
28
29
30
31
32
33
34
35
36
37
38
39
40
41
42
43
44
45
46
47
48
49
50
51
52
53
54
55
56
57
58
59
60



POLDIRAD reflectivity PPI observations of the heavy precipitation isolated cell on July 15, 2007 (IOP 8b) at 14:20, 14:40, 15:00, and 15:20 UTC, respectively. The colour scale indicates the reflectivity from -10 to 60 DBz.

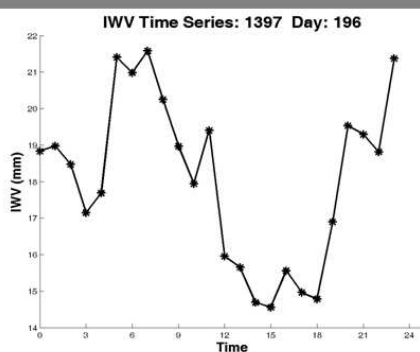
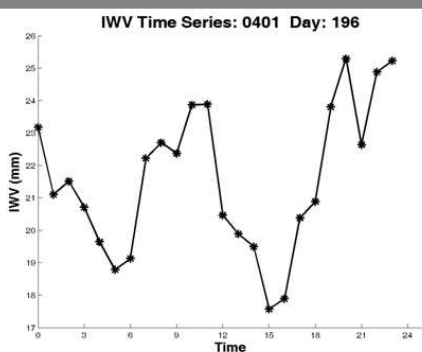
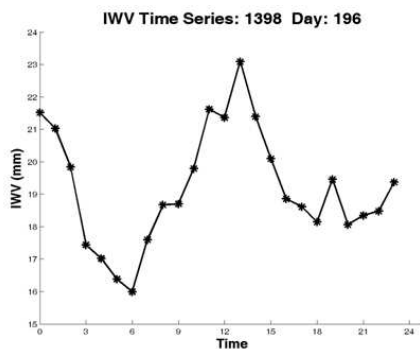
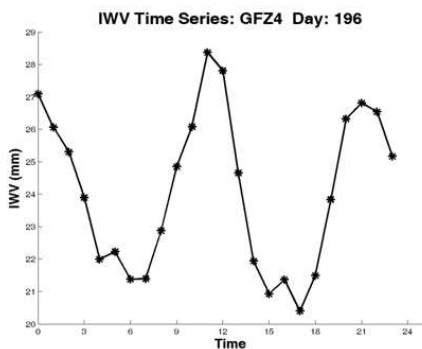


1
2
3
4
5
6
7
8
9
10
11
12
13
14
15
16
17
18
19
20
21
22
23
24
25
26
27
28
29
30
31
32
33
34
35
36
37
38
39
40
41
42
43
44
45
46
47
48
49
50
51
52
53
54
55
56
57
58
59
60



GPS IWV 2-D fields (left column) and tomography horizontal water vapour density fields at the 1000 m height layer (right column) from 13:00 to 15:00 UTC on July 15, 2007 (IOP 8b). The IWV scale goes from 5 to 40 mm and the water vapour density scale goes from 4 to 14 g/m³. The black circle indicates the area of convective activity seen on the radar display of Figure 2.

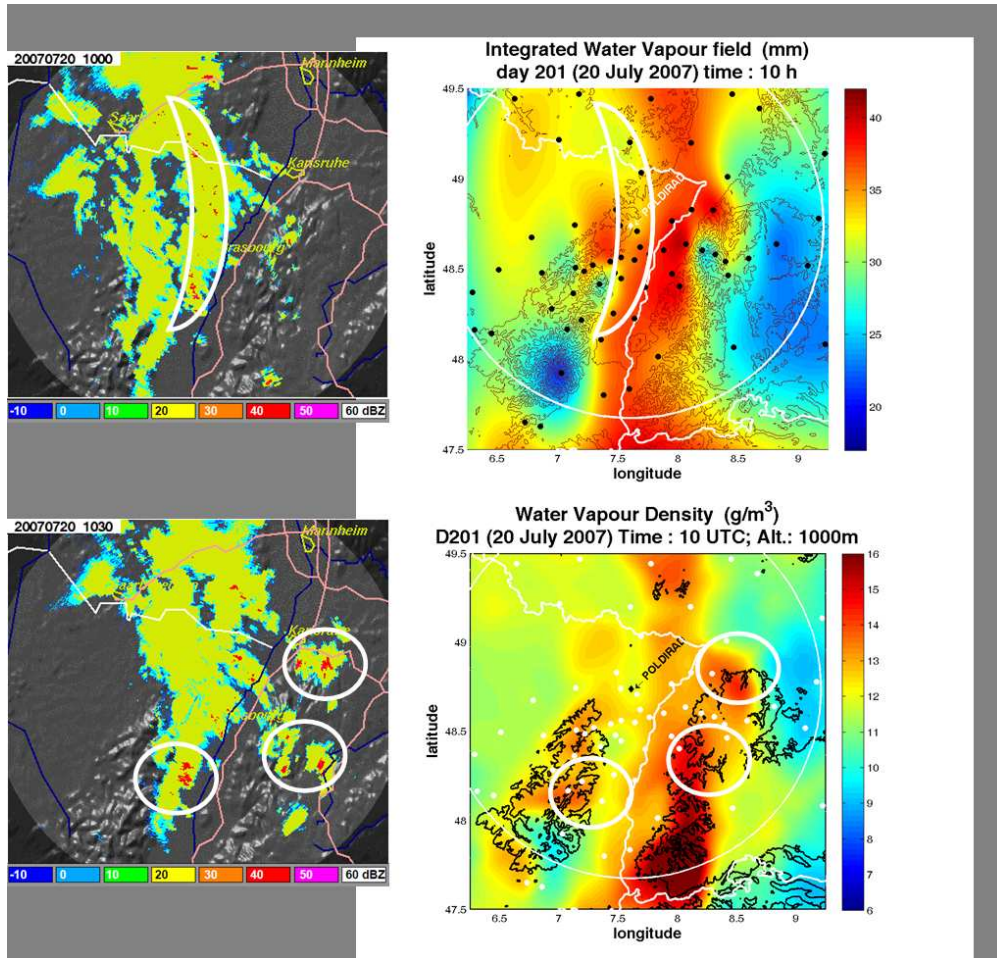
1
2
3
4
5
6
7
8
9
10
11
12
13
14
15
16
17
18
19
20
21
22
23
24
25
26
27
28
29
30
31
32
33
34
35
36
37
38
39
40
41
42
43
44
45
46
47
48
49
50
51
52
53
54
55
56
57
58
59
60



IWV time series for July 15, 2007 (IOP 8b: Day 196) for the four surrounding GPS stations around the area of convective activity at 15:00 UTC in the Black Forest (black circle on the previous figure). Positions on the plots correspond to the relative cardinal positions of the GPS stations.

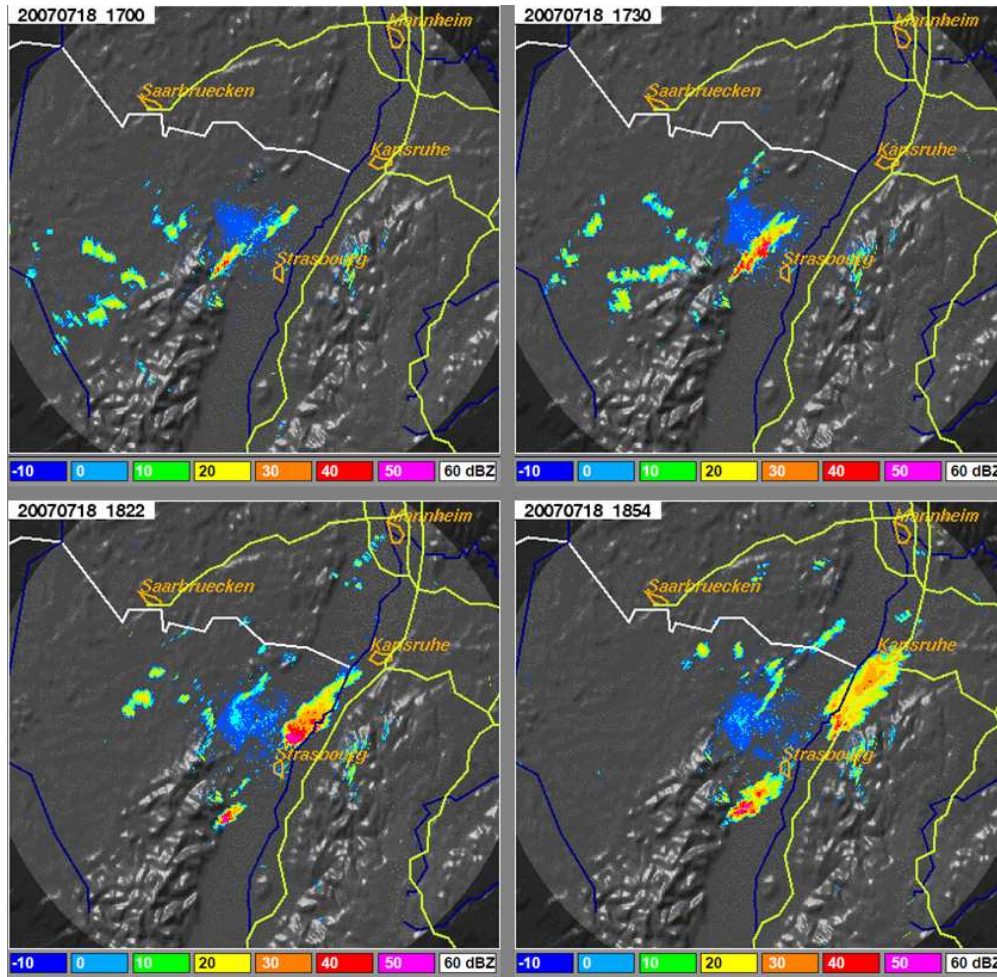
Review

1
2
3
4
5
6
7
8
9
10
11
12
13
14
15
16
17
18
19
20
21
22
23
24
25
26
27
28
29
30
31
32
33
34
35
36
37
38
39
40
41
42
43
44
45
46
47
48
49
50
51
52
53
54
55
56
57
58
59
60



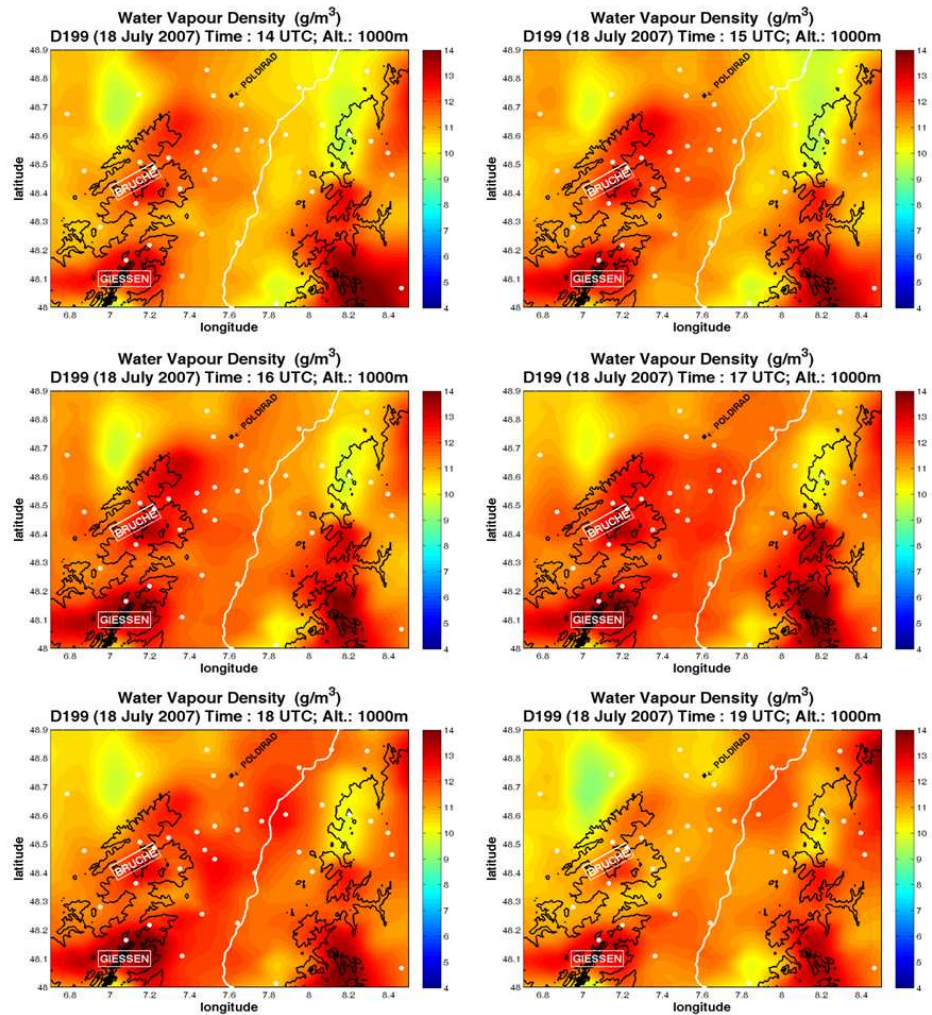
POLDIRAD reflectivity PPI observations on July 20, 2007 (IOP 9c) at 10:00, and 10:30 UTC, respectively (left column) and GPS IWV field (top right panel) and tomography horizontal water vapour density field for the 1000 m (bottom right panel) height layer at 10:00 UTC on July 20, 2007 (IOP 9c). The radar reflectivity scale goes from -10 to 60 DBz. The IWV scale goes from 17 to 42 mm and the water vapour density scale goes from 6 to 16 g/m^3 .

1
2
3
4
5
6
7
8
9
10
11
12
13
14
15
16
17
18
19
20
21
22
23
24
25
26
27
28
29
30
31
32
33
34
35
36
37
38
39
40
41
42
43
44
45
46
47
48
49
50
51
52
53
54
55
56
57
58
59
60



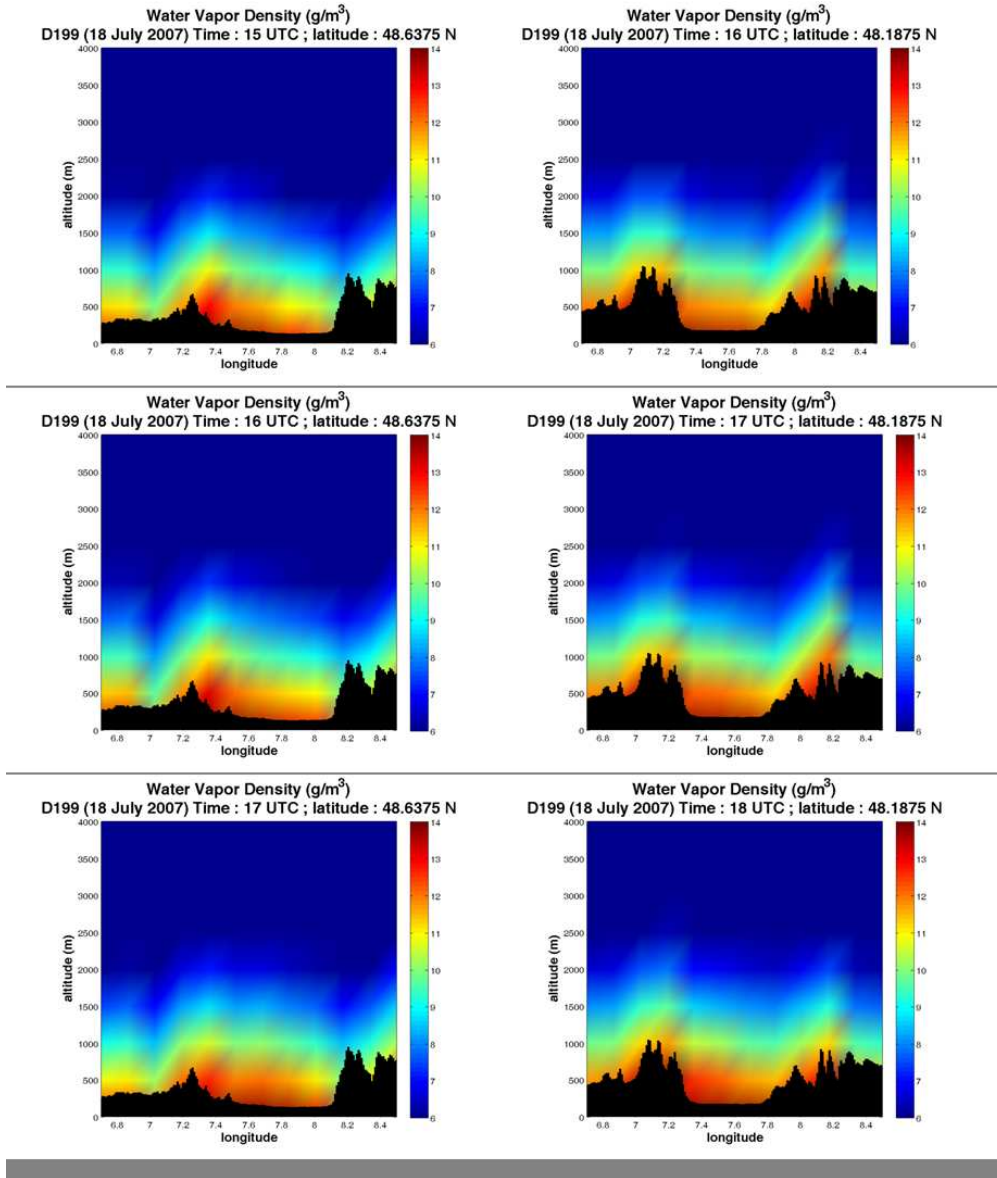
POLDIRAD reflectivity PPI observations on July 18, 2007 (IOP 9a) at 17:00, 17:30, 18:22, and 18:54 UTC, respectively. The colour scale indicates the reflectivity from -10 to 60 DBz.

1
2
3
4
5
6
7
8
9
10
11
12
13
14
15
16
17
18
19
20
21
22
23
24
25
26
27
28
29
30
31
32
33
34
35
36
37
38
39
40
41
42
43
44
45
46
47
48
49
50
51
52
53
54
55
56
57
58
59
60



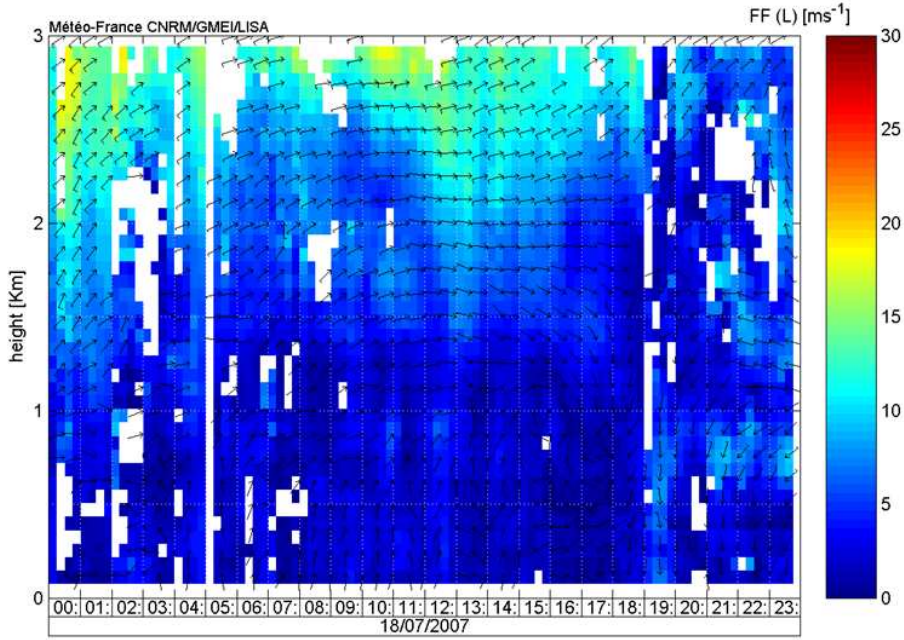
GPS tomography horizontal water vapour density fields for the 1000 m height layer from 14:00 to 19:00 UTC, on July 18, 2007 (IOP 9a). The water vapour density scale goes from 4 to 14 g/m³. The Bruche and Giessen valleys are indicated.

1
2
3
4
5
6
7
8
9
10
11
12
13
14
15
16
17
18
19
20
21
22
23
24
25
26
27
28
29
30
31
32
33
34
35
36
37
38
39
40
41
42
43
44
45
46
47
48
49
50
51
52
53
54
55
56
57
58
59
60



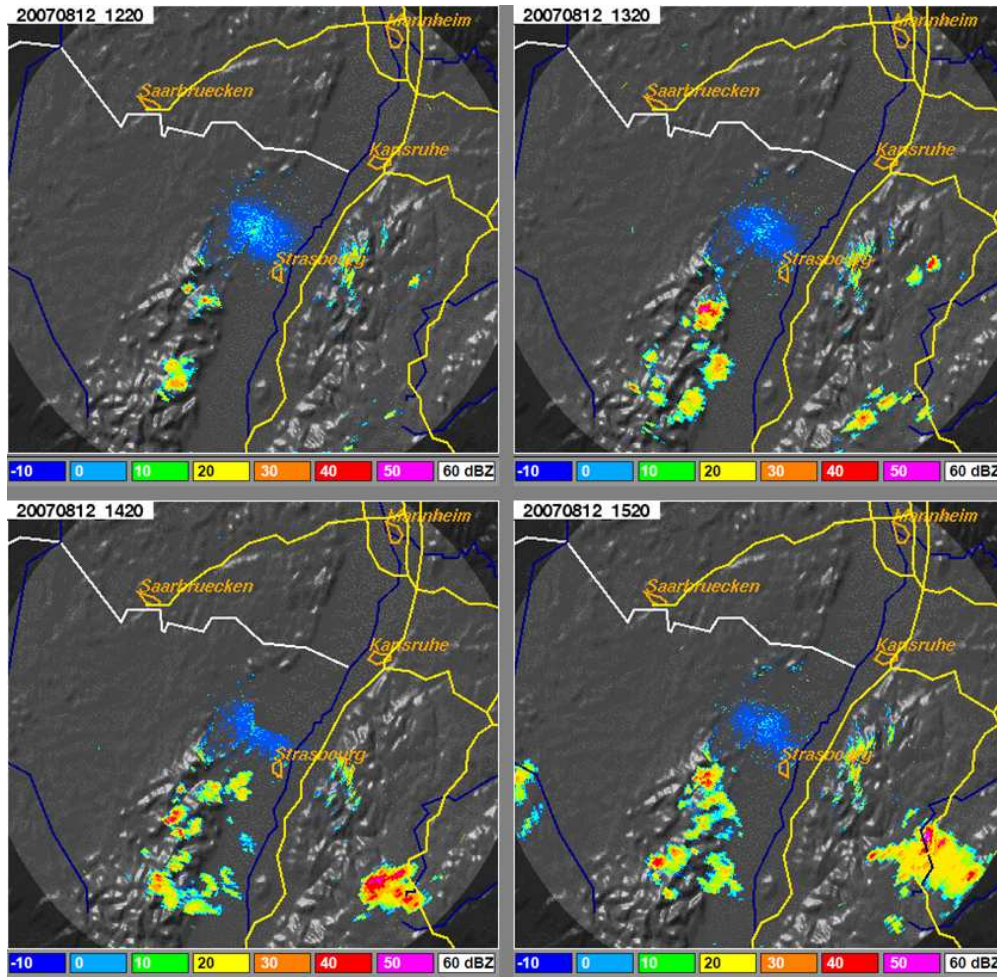
GPS tomography vertical water vapour density cross-sections at constant latitude 48.64° N (left column) and 48.19° N (right column) from 15:00 to 17:00 and 16:00 to 18:00 UTC, respectively, on July 18, 2007 (IOP 9a). The water vapour density scale goes from 6 to 14 g/m³.

1
2
3
4
5
6
7
8
9
10
11
12
13
14
15
16
17
18
19
20
21
22
23
24
25
26
27
28
29
30
31
32
33
34
35
36
37
38
39
40
41
42
43
44
45
46
47
48
49
50
51
52
53
54
55
56
57
58
59
60



Supersite Vosges UHF wind profiler time/height plot for July 18, 2007 (IOP 9a). Colour scale indicates wind amplitude in m/s while arrows indicate wind direction.

Review

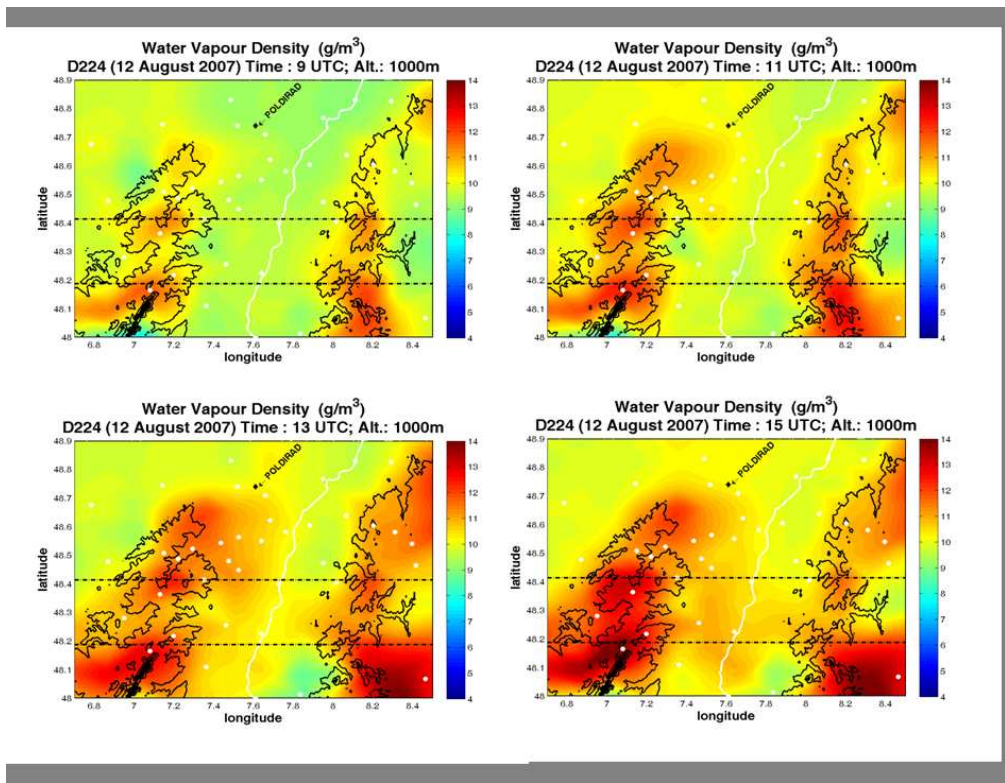


POLDIRAD reflectivity PPI observations on August 12, 2007 (IOP 15a) at 12:20, 13:20, 14:20 and 15:20 UTC, respectively. The colour scale indicates the reflectivity from 10 to 60 DBz.



1
2
3
4
5
6
7
8
9
10
11
12
13
14
15
16
17
18
19
20
21
22
23
24
25
26
27
28
29
30
31
32
33
34
35
36
37
38
39
40
41
42
43
44
45
46
47
48
49
50
51
52
53
54
55
56
57
58
59
60

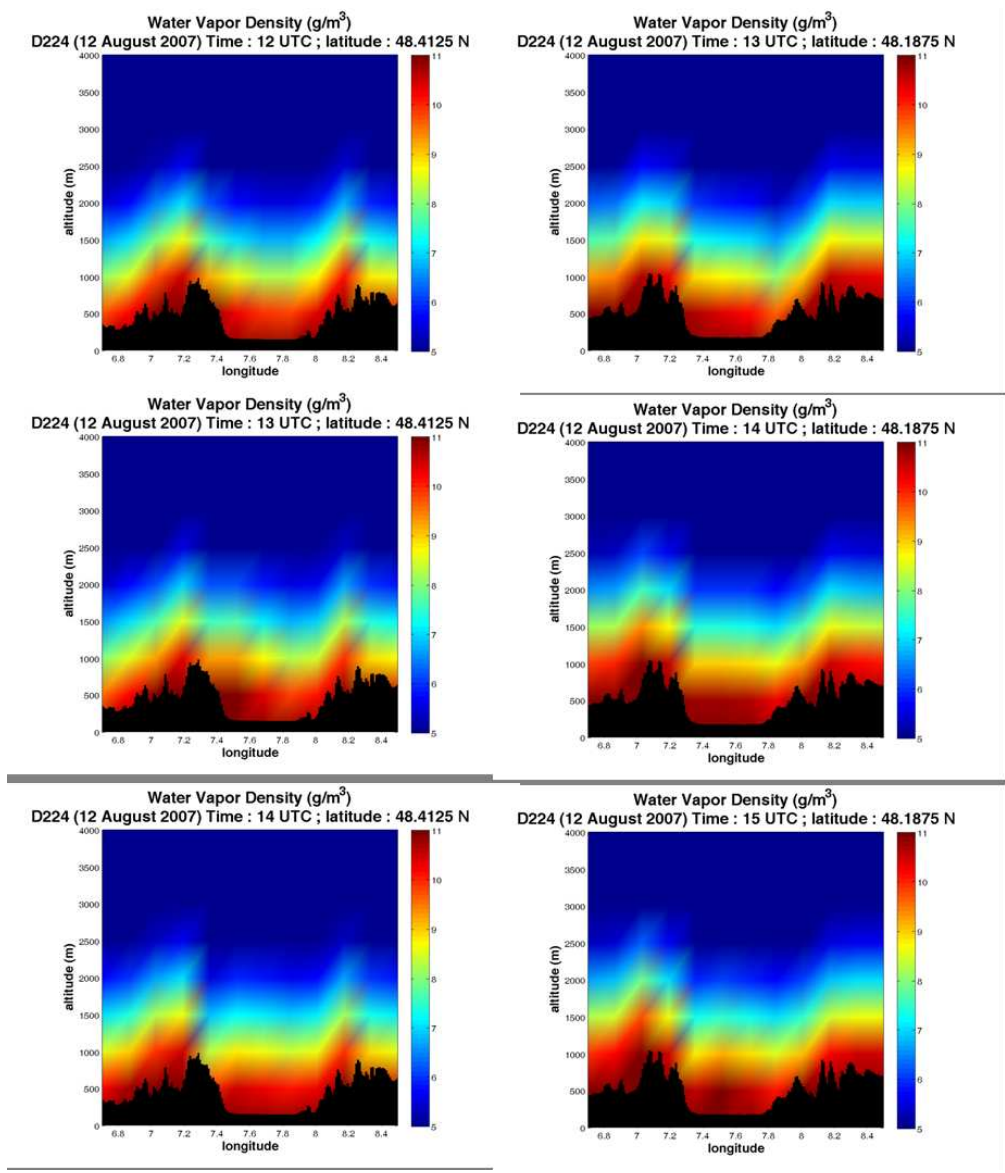
1
2
3
4
5
6
7
8
9
10
11
12
13
14
15
16
17
18
19
20
21
22
23
24
25
26
27
28
29
30
31
32
33
34
35
36
37
38
39
40
41
42
43
44
45
46
47
48
49
50
51
52
53
54
55
56
57
58
59
60



GPS tomography horizontal water vapour density fields for the 1000 m height layer for the 9:00, 11:00, 13:00, and 15:00 UTC time frames, respectively, on August 12, 2007 (IOP 15a). The water vapour density scale goes from 4 to 14 g/m³. The dash lines indicate the vertical cross-sections of Figure 9b.

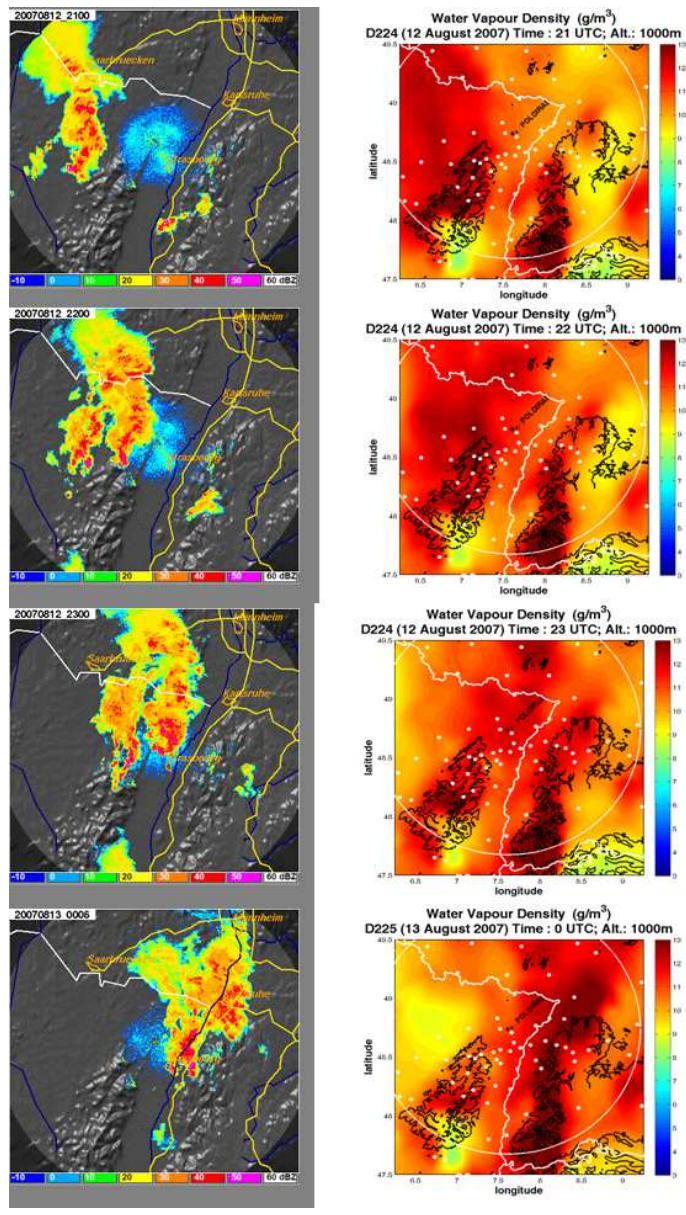
view

1
2
3
4
5
6
7
8
9
10
11
12
13
14
15
16
17
18
19
20
21
22
23
24
25
26
27
28
29
30
31
32
33
34
35
36
37
38
39
40
41
42
43
44
45
46
47
48
49
50
51
52
53
54
55
56
57
58
59
60

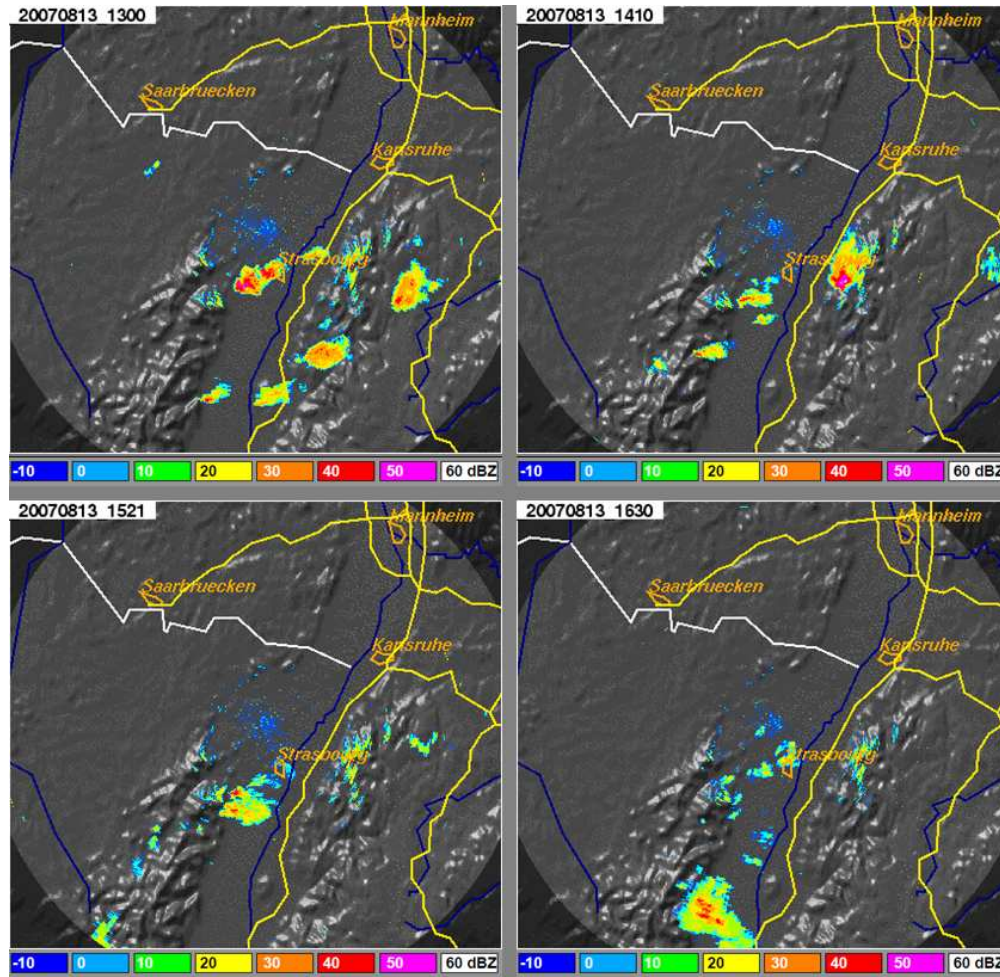


GPS tomography vertical water vapour density cross-sections at constant latitude 48.41° N (left column) and 48.19° N (right column) from 12:00 to 14:00 and 13:00 to 15:00 UTC, respectively, on August 12, 2007 (IOP 15a). The water vapour density scale goes from 5 to 11 g/m³.

1
2
3
4
5
6
7
8
9
10
11
12
13
14
15
16
17
18
19
20
21
22
23
24
25
26
27
28
29
30
31
32
33
34
35
36
37
38
39
40
41
42
43
44
45
46
47
48
49
50
51
52
53
54
55
56
57
58
59
60



POLDIRAD reflectivity PPI observations on August 12, 2007 at 21:00, 22:00, 23:00, and August 13, 2007 at 00:00 UTC (IOP 15) respectively (left column) and GPS tomography horizontal water vapour density fields at the 1000 m height layer for the same times (right column). The radar reflectivity scale goes from -10 to 60 DBz. The water vapour density scale goes from 3 to 13 g/m³.

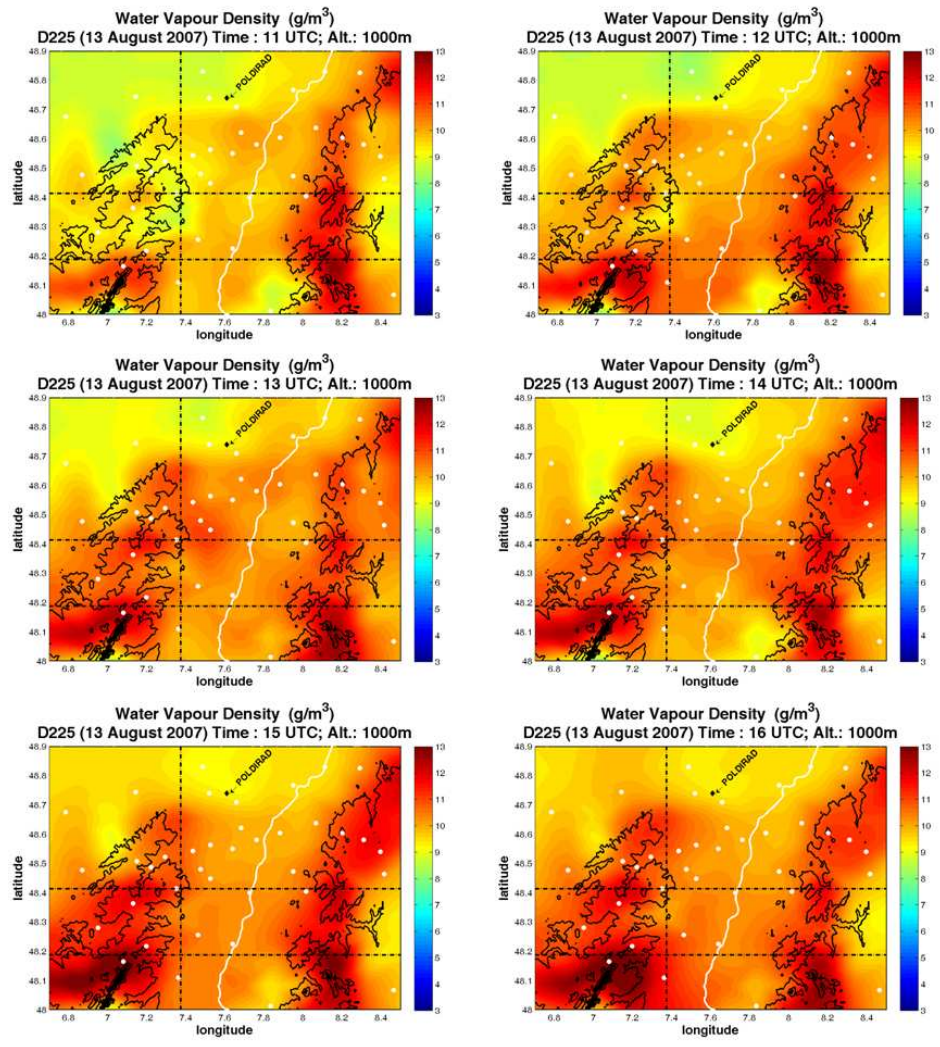


POLDIRAD reflectivity PPI observations of isolated cells on August 13, 2007 (IOP 15b) at 13:00, 14:10, 15:21, and 16:30 UTC, respectively. The colour scale indicates the reflectivity from -10 to 60 DBz.



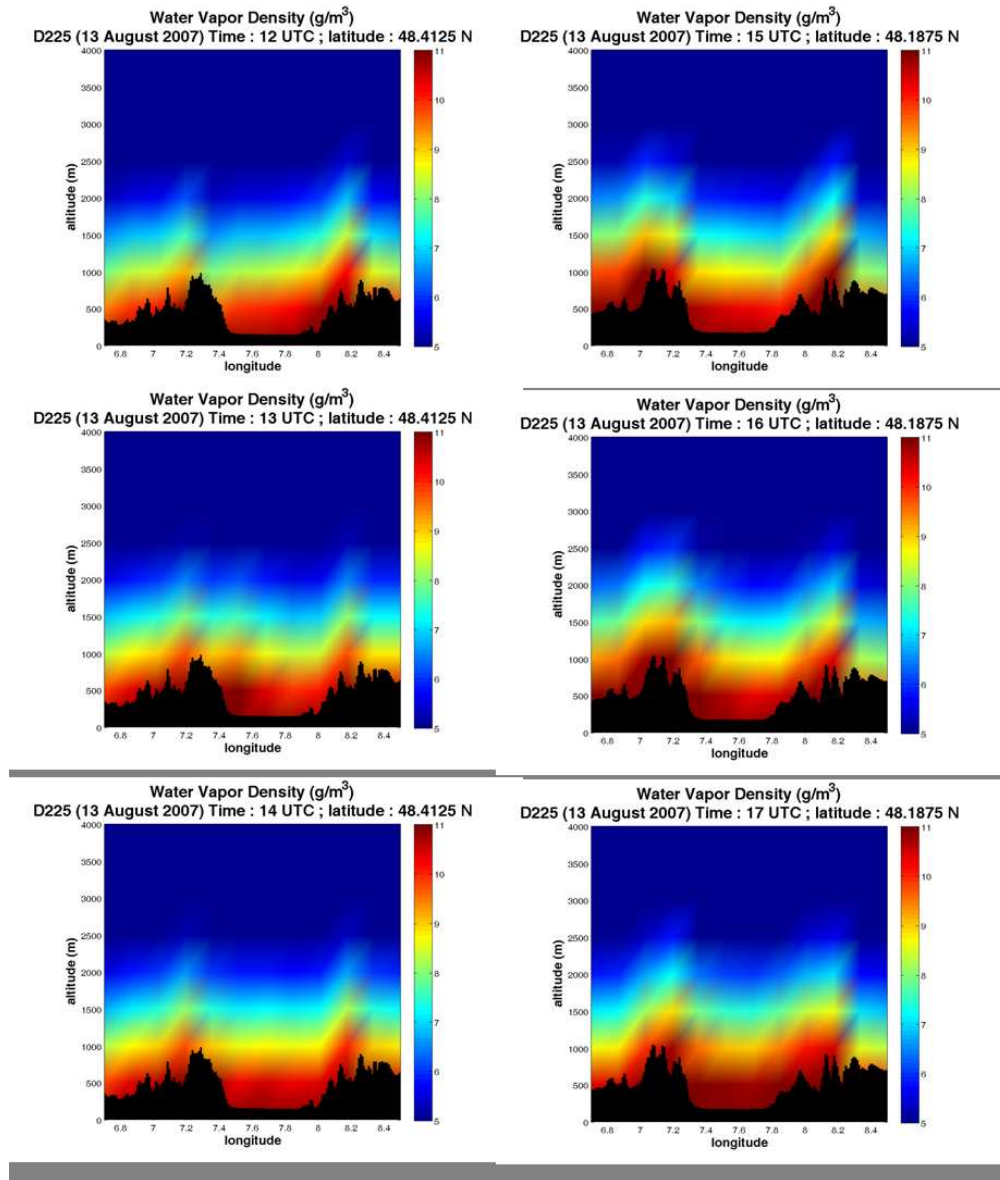
1
2
3
4
5
6
7
8
9
10
11
12
13
14
15
16
17
18
19
20
21
22
23
24
25
26
27
28
29
30
31
32
33
34
35
36
37
38
39
40
41
42
43
44
45
46
47
48
49
50
51
52
53
54
55
56
57
58
59
60

1
2
3
4
5
6
7
8
9
10
11
12
13
14
15
16
17
18
19
20
21
22
23
24
25
26
27
28
29
30
31
32
33
34
35
36
37
38
39
40
41
42
43
44
45
46
47
48
49
50
51
52
53
54
55
56
57
58
59
60



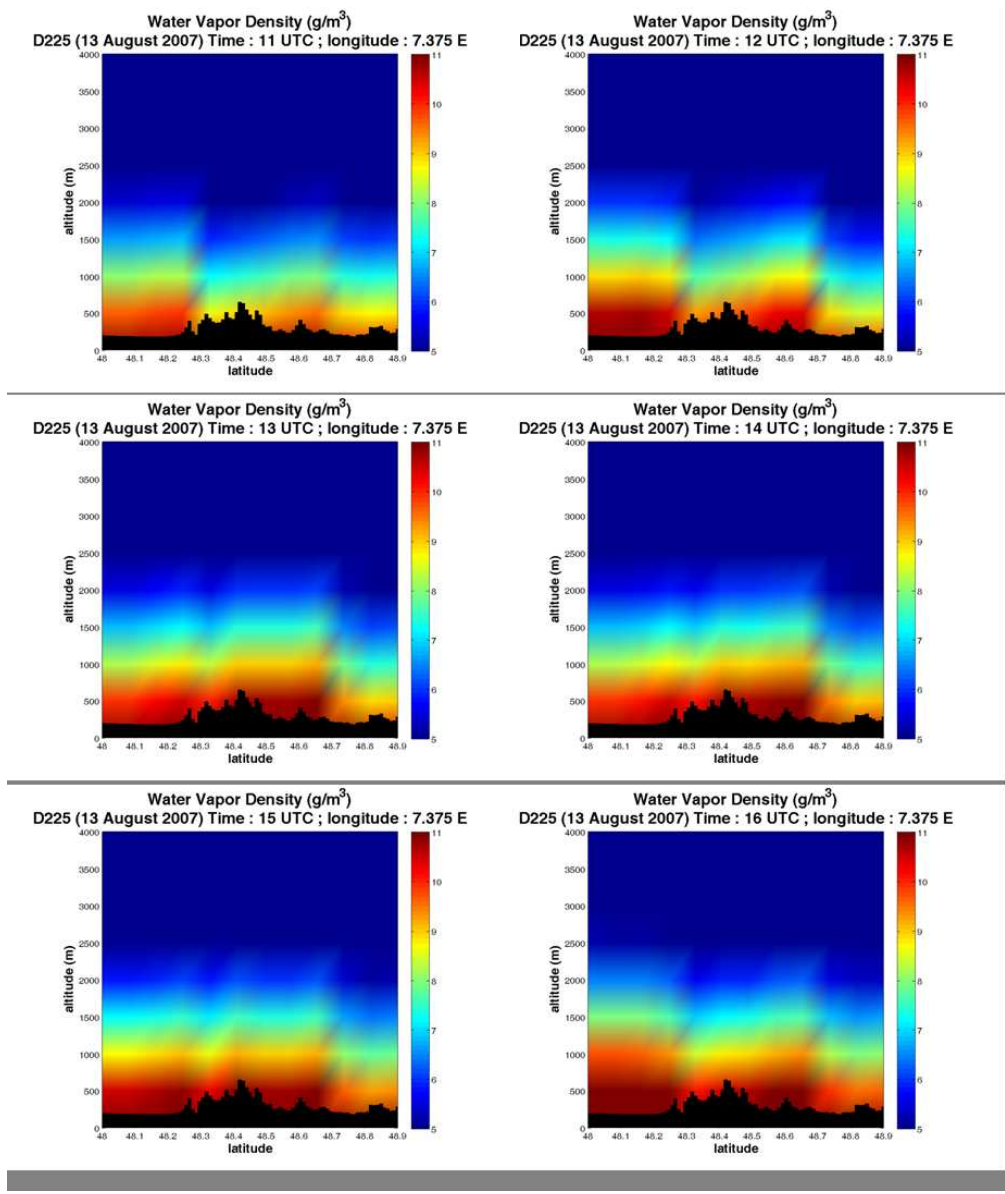
GPS tomography horizontal water vapour density cuts for the 1000 m height layer from 11:00 to 16:00 UTC, on August 13, 2007 (IOP 15b). The water vapour density scale goes from 3 to 13 g/m³. The dash lines indicate the vertical cross-sections of Figure 12b and 12c.

1
2
3
4
5
6
7
8
9
10
11
12
13
14
15
16
17
18
19
20
21
22
23
24
25
26
27
28
29
30
31
32
33
34
35
36
37
38
39
40
41
42
43
44
45
46
47
48
49
50
51
52
53
54
55
56
57
58
59
60



GPS tomography vertical water vapour density cross-sections at constant latitude 48.41°N (left column) and 48.19°N (right column) from 12:00 to 14:00 and 15:00 to 17:00 UTC, respectively, on August 13, 2007 (IOP 15b). The water vapour density scale goes from 5 to 11 g/m^3 .

1
2
3
4
5
6
7
8
9
10
11
12
13
14
15
16
17
18
19
20
21
22
23
24
25
26
27
28
29
30
31
32
33
34
35
36
37
38
39
40
41
42
43
44
45
46
47
48
49
50
51
52
53
54
55
56
57
58
59
60



GPS tomography vertical water vapour density cross-sections at constant longitude 7.34° E from 11:00 to 16:00 UTC, on August 13, 2007 (IOP 15b). The water vapour density scale goes from 5 to 11 g/m^3 .